

Constructing a Linear Paul Trap System for
Measuring Time-variation of the
Electron-Proton Mass Ratio

Shenglan Qiao

Advisor: Professor David Hanneke
May 6, 2013

Submitted to the
Department of Physics of Amherst College
in partial fulfilment of the
requirements for the degree of
Bachelors of Arts with honors

© 2013 Shenglan Qiao

Abstract

Attempts at quantum theories of gravity as well as tantalizing astrophysics results suggest a need to examine the stability of fundamental constants with respect to position and time. We have chosen to investigate time-variation of the electron-proton mass ratio (μ), as this dimensionless number is critical to our understanding of fundamental interactions. We plan to observe shifts in certain energy levels sensitive to temporal changes of μ in a molecular ion, possibly $^{16}\text{O}_2^+$, via quantum logic spectroscopy. This technique requires co-trapping the molecular ion with an atomic ion, specifically $^9\text{Be}^+$ in our proposed experiment. Trapping of the ions gives us very long interrogation time and thus higher precision through the frequency-time uncertainty relation. Quantum logic spectroscopy allows us to sympathetically cool the molecular ion with the atomic ion as well as to prepare and detect its internal states, which are more sensitive to changes of μ . Our proposed experiment, therefore, allows us to not only extract $d\mu/dt$ from changes in the frequencies of certain transitions in the molecular ion but also to develop a high-precision spectroscopy method using molecules.

This thesis focuses on building the linear Paul trap system that will co-trap the two ions in an approximately harmonic potential well. We have designed and constructed the trap electrodes and are in the process of putting the rest of the system together. We also provide some preliminary designs, which include a procedure and instrumentation to create ultra-high vacuum, circuits for the signals to the trap electrodes, and optics for imaging the trapped ions. Some of these designs are ready for actual construction and assembling of the apparatus; others, for which we have offered our thoughts and questions, need more polishing. Besides designs for the hardware, we also present the motivations behind our experimental goals and the methods to achieve them so that future generations of thesis writers can keep their eyes on the prize and continue to work towards it.

Acknowledgements

I would like to thank my thesis advisor, Professor David Hanneke, for being a wonderful mentor. I would not have learnt so much from completing this project without his constant support. Jim Kubasek, our machinist, has also helped me tremendously. I would not have done nearly as much if he did not generously and patiently share his expertise with me. I am also grateful to all the faculty members in the department for their instruction, advice, and guidance throughout my four years at Amherst College. Furthermore, my thesis would not have been possible without the generous funding from the Dean of the Faculty and the Research Corporation. Last but not least, I would like to thank His Holy Fluffiness the Squirrel God, for all the divine revelations I received during the bleakest hours of my senior year.

Contents

1	The Journey Begins	2
2	Linear Paul Trap: Theory, Design and Construction	6
2.1	Linear Paul Trap Theory	7
2.1.1	The Classical Picture: Equations of Motion	10
2.1.2	Solutions to Mathieu's Equation and the Stability Region in a-q Space	11
2.2	Design Considerations	15
2.2.1	Stability in m-Q space	15
2.2.2	Pseudopotentials and Trap Frequencies	19
2.3	Construction of the Trap	23
2.4	Final Thought: The Geometric Constant	28
3	Putting it All Together: the Rest of the Paul Trap System	33
3.1	Overview	34
3.2	Generating the Trapping Potential	35
3.2.1	RF Power Supply	37
3.2.2	DC Power Supply	40
3.3	Creating Ultra-high Vacuum	41
3.3.1	Pumping of the Vacuum System	42
3.3.2	Sources of Gas in Vacuum	44
3.3.3	Choice of UHV pumps	47
3.4	Imaging System	50
4	Our Final Destination: Measuring the Time-variation of Electron-Proton Mass Ratio	54
4.1	Theoretical Motivations	55
4.2	The Stability of μ	57
4.2.1	Bounds from Astronomical Data	58
4.2.2	Bounds from Laboratory Spectroscopic Data	60

4.3	Search for the Most Suitable Diatomic Molecular Ion	63
4.4	Quantum Logic Spectroscopy	70
4.4.1	How it works	70
4.4.2	Initial State Preparation	73
5	Not A Conclusion	78
A	Machined Linear Paul Trap Drawings	81
B	Mathematica Notebook for Helical Resonator	93
C	Inventory for Vacuum System	99

List of Figures

2.1	Cartoons of electrodes for an ideal Paul trap	9
2.2	Stability regions in an arbitrary dimension	13
2.3	Stability region for confinement in the a-q space	14
2.4	Stability region in m-Q space	17
2.5	Electrodes of the actual linear Paul trap	25
2.6	Cartoon of a real linear Paul trap	30
3.1	A schematic of the Paul trap system	35
3.2	A schematic of the DC and RF power supplies	36
3.3	A schematic diagram of the helical resonator	38
3.4	An example of virtual leak	46
3.5	A “cross-section” of two point sources	52
4.1	Quantum logic spectroscopy	73
4.2	Rotational cooling of the spectroscopy ion	75

Chapter 1

The Journey Begins

“I am going on an adventure!” — Bilbo Baggins, *The Hobbit*

This thesis is the beginning of a long and difficult but also exciting and rewarding journey. Although the eighty-or-so pages that you are about to read are a somewhat impersonal, academic and technical account of the first few episodes of this adventure, in this introduction I am going to speak to you, the reader, directly, as if I am talking to you face-to-face and waving my arms. This is the only way I can think of to sell this adventurous scheme to you and entice you to read the rest of my thesis. Moreover, since we are probing fundamental laws of physics here, the final destination of our journey is too attractive to hide behind the veil of third-person pronouns. Therefore, with the most animated language and impassioned vocabulary, I introduce to you our proposed journey and the role I have played in it.

We begin our journey with an end in mind, which is to answer the question if the electron-proton mass ratio, μ for short, varies with time. Consid-

ering that both of those masses are “fundamental constants”, it is a rather peculiar question to ask. We have, however, ample reasons to suspect that “fundamental constants” do change as functions of position and time. Certain unified theories of fundamental interactions require “fundamental constants” to change. Previous research efforts have also collected data that open serious questions on the stability of μ . Sections 4.1 and 4.2 will be able tell you all about these reasons that motivate us to probe the time-dependence of μ . Furthermore, the two possible answers to our question, “yes” and “maybe”, are both coveted treasures. If our experiment eventually allows us to see some evidence of time-variation in the electron-to-proton mass ratio, then we will confirm some of the theories that predict it; on the other hand, if we manage to further limit the size of the variation, we will constrain speculative theories. Either way, this journey will take us to an appealing final destination.

Furthermore, we think we know the way to our final destination and the view on the road is not going to be bad at all. We know that μ determines the sizes of rovibrational transitions in diatomic molecules and shifts in their frequencies over time are manifestations of the time-variations of μ . Some of these transitions are particularly sensitive, producing larger frequency shifts that are easier to measure very precisely. Also, the techniques for measuring frequencies of transitions in atoms and molecules, also known as high-precision frequency metrology, have been developed by some of the brightest minds in physics for many years. We are not re-inventing the wheel here, but to get to our final destination, we need to do it better. The method we propose here is a recent technique, quantum logic spectroscopy, adopted from the land of

quantum information processing, which performs the high-precision frequency metrology we want to do with two ions, one atomic and the other molecular. This new technique will allow us to prepare and detect the internal states of the molecular ion, which may be more sensitive to changes in μ . Section 4.4 contains a detailed account on our experimental method. As promised earlier, the view on the road itself is an attraction of the journey; even though it may take years for us to collect data on the time-variation of μ , we will have developed and polished a new and presumably better spectroscopy method with diatomic molecular ions, which has never been done before.

Having full confidence in this adventure being a rewarding one, we began to traverse the first few miles of the journey. This thesis is a part of the efforts to put together the apparatus that will perform the spectroscopy experiment. It involves designing and constructing a linear Paul trap system that will contain the two ions we hope to use for high-precision frequency metrology. A linear Paul trap is a device that confines charged particles, the ions for spectroscopy in our case, using an oscillating electric field. Trapping the ions gives us very long interrogation time and thus higher precision through the frequency-time uncertainty relation. Chapter 2 focuses exclusively on the trap we have designed and built. Chapter 3 will present preliminary designs, ideas, and unanswered questions on the rest of the Paul trap system yet to be constructed. Given the arbitrary time-frame of a senior thesis, however, this is as far as I could take it.

Nevertheless, I have written the following chapters with the next generation of adventurers in mind and with the hope that they will help them a little

further beyond the due date of my thesis. In other words, instead of simply being an account of what I have done, the following chapters are supposed to be read like a guidebook, or perhaps an incomplete but still somewhat informative map. Chapter 2 describes the theory of the linear Paul trap and design considerations we have had while constructing it; Section 2.4 suggests a geometric factor of the trap that will be interesting to characterize once the entire system is up and running. Chapter 3 contains designs of other components of the Paul trap systems. Some of these designs are ready-to-use “recipes”; others need to have more thinking put into them. Chapter 3 also include what I believe to be the next steps to take and some potential potholes on the road. Additionally, if the future adventurers ever need a reminder of our final destination and its many attractions or desire the “big picture” of this long and strenuous road trip, they should hopefully find Chapter 4 a useful read or at least a helpful pointer to relevant articles in the existing literature. Finally, apart from the appendices, I have included a handful of Mathematica notebooks¹ that will perform certain calculations in Chapters 2 and 3; they are meant to save the reader the trouble to reconstruct them from my written words and use them to help design pieces of apparatus yet to be built.

Now with this “guidebook” in hand, it is time to buckle up and let the journey begin!

¹One of the notebooks that calculates the geometric parameters of the helical resonator is included in Appendix B. The others are in the disc attached to this thesis. One does not have to refer to the notebooks, with the exception of the one in Appendix B, in order to follow this thesis.

Chapter 2

Linear Paul Trap: Theory, Design and Construction

An ideal Paul trap generates an oscillating electric field to confine charged particles. The average force on a charged particle in such a field, taken over many oscillations, can be convergent towards the center of the trap, which coincides with the point of the lowest average potential, leading to confinement; in other cases, it is divergent, leading to the loss of the particle. With the appropriate amplitude and frequency, the oscillating potential can result in a time-averaged convergent force towards the trap center in two out of the three spatial dimensions. A DC potential can then be added to provide confinement in the third dimension.

Wolfgang Paul, after whom this method of ion trapping is named, demonstrated this dynamic stabilization with an analogous mechanical device shaped like a saddle [1]. If one simply places a ball near the saddle point of the device,

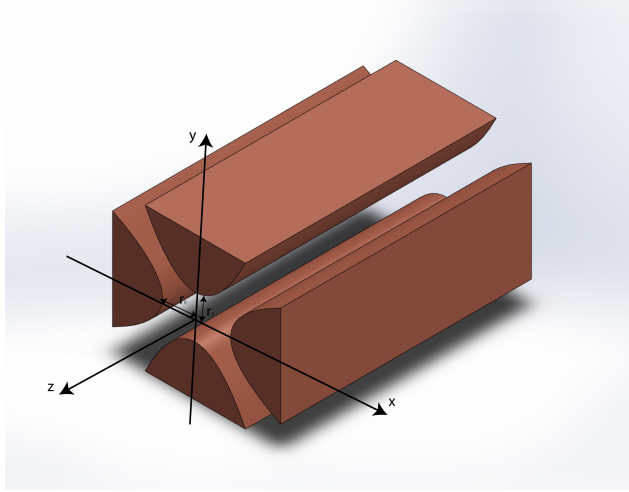
it will roll off the surface. If the device is rotating at an appropriate frequency around the normal axis through the saddle point, however, the ball will stay on the surface while making small oscillations around the axis of rotation with a frequency smaller than that of the saddle's rotation. There is an upper and a lower bound to the range of frequencies that will allow the ball to stay on the saddle. Besides providing this intuitive explanation, this chapter explains the theory behind the linear Paul trap in mathematical details¹. After delineating the basic theory, it will discuss the design considerations as consequences of our mathematical model. Finally, it will present the specifications of the actual trap we have constructed.

2.1 Linear Paul Trap Theory

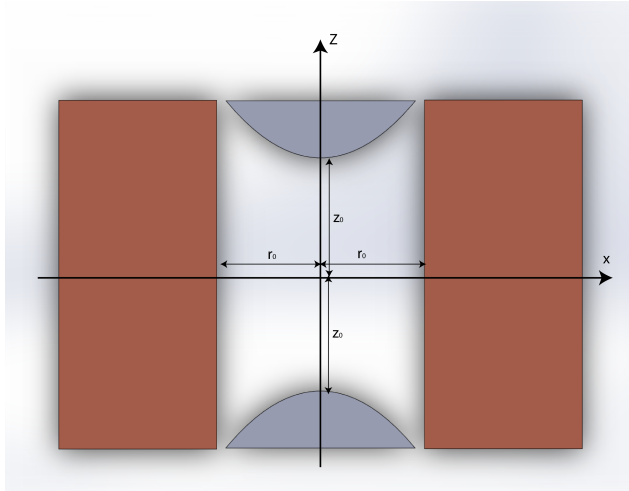
We begin examining the theory of ion trapping by assuming some kind of idealized linear Paul trap. An ideal linear Paul trap generates a potential Φ that takes the form of $\Phi = Ax^2 + By^2 + Cz^2$. It is able to do so by having four infinitely long rod electrodes and two endcap electrodes (Figure 2.1). The cross-section of the rod electrodes in the xy -plan is shaped exactly like the equipotential surfaces of the quadrupole field in the same plane (Figure 2.1 (a)). The endcap electrodes are tapered so that they come close to the center of the trap (Figure 2.1 (b)). By applying an oscillating radio frequency (RF) potential to the four rod electrodes and a DC potential to the endcap electrodes, one can generate a cylindrically symmetric (thus linear in the sense that the

¹For more detailed theoretical treatments of this subject, see refs [1], [2], and [3] on which we have based all of our theoretical discussions in this chapter, with the exception of Section 2.2.1.

field is not oscillating on the z -axis) oscillating field in which the RF potential provides the radial confinement (confinement in the xy -plane) of the particle while the DC potential takes care of the axial confinement (confinement in the z -axis).



(a) Rod electrodes. Endcap electrodes are not shown in this diagram for clarity.



(b) Endcap electrodes, seen as a cross-section in the xz -plane. They are colored grey.

Figure 2.1: Cartoons of electrodes for an ideal Paul trap. The electrodes are shaped as such to generate the ideal quadrupole potential. For an ideal linear Paul trap, the cross-section of the rod electrodes in the xy -plane should look like that of an asymptotic cone [2].

It is easy to see that in order to satisfy the Laplacian $\nabla^2\Phi = 0$, it must be true that $A + B + C = 0$. Subsequently, we can derive that the potentials, Φ_{rod} and Φ_{end} , generated by the rod electrode and the endcap electrodes re-

spectively [2]. Given that a RF potential $V_0 \cos \Omega t$ is applied to two of the rod electrodes while the other two are held at RF ground, and the DC potential applied to the endcap electrodes is U_0 , we have

$$\Phi_{rod} = \frac{V_0}{2} \cos \Omega t \left(1 + \frac{x^2 - y^2}{r_0^2} \right) \quad (2.1)$$

and

$$\Phi_{end} = \frac{U_0}{z_0^2} [z^2 - \frac{1}{2}(x^2 + y^2)]. \quad (2.2)$$

Consequently, the combined potential Φ inside the ideal linear Paul trap is just the superposition of Φ_{rod} and Φ_{end} . With equations 2.1 and 2.2, we are now ready to obtain the classical equations of motion of charged particles inside this potential.

2.1.1 The Classical Picture: Equations of Motion

Applying Newton's Second Law and given that m is the mass of the particle and Q its charge, in the z-direction, we simply have

$$\frac{d^2 z}{dt^2} m = -\frac{2QU_0}{z_0^2} z, \quad (2.3)$$

which is, with an appropriate sign for U_0 , the equation of motion for simple harmonic motion. In other words, confinement on the z-axis depends only on the choice of sign for the DC potential applied to the endcap electrodes; the angular frequency of oscillation in the axial direction is therefore $\omega_z = \sqrt{\frac{2QU_0}{z_0^2 m}}$.

Similarly, the equation of motion in the x-direction is

$$\frac{d^2x}{dt^2}m = -Q \left(\frac{V_0}{r_0^2} \cos \Omega t - \frac{U_0}{z_0^2} \right) x. \quad (2.4)$$

Simple algebraic manipulations turns equation 2.4 into the canonical form of Mathieu's equations with parameters (a_x, q_x) , which is

$$\frac{d^2x}{d\xi^2} + (a_x - 2q_x \cos 2\xi)x = 0$$

where

$$\xi = \frac{\Omega t}{2}, \quad a_x = -\frac{4QU_0}{\Omega^2 m z_0^2}, \quad \text{and} \quad q_x = -\frac{2QV_0}{\Omega^2 m r_0^2}. \quad (2.5)$$

Solutions to the Mathieu's equation are standard; only certain combinations of values for the parameters (a_x, q_x) will lead to solutions that correspond to confinement of the particle in the x direction. The situation is similar in the y direction with $a_y = a_x$ and $q_y = -q_x$. As a result, requiring confinement in both x- and y-directions limit the set of values for (a_i, q_i) ($i = 1, 2$ for x and y respectively) to a bounded region, known as the stability region, in a-q space.

2.1.2 Solutions to Mathieu's Equation and the Stability Region in a-q Space

In order to find this stability region, we have to first look at the general solution to Mathieu's equation. According to Floquet's theorem, solutions to the equation are linear combinations of two functions, $u_1(\xi) = e^{\mu\xi}\phi(\xi)$ and

$u_2(\xi) = e^{-\mu\xi}\phi(-\xi)$, where ϕ is a periodic function, and $\mu = \alpha + \beta i$, where α and β are $\text{Re}(\mu)$ and $\text{Im}(\mu)$ respectively. This is true if and only if $\alpha \neq 0$ or $\alpha = 0$ and β is not an integer. Otherwise, another solution has to be found to combine with one of the Floquet solutions [2]. If $\alpha \neq 0$, however, either u_1 or u_2 blows up as $\xi \rightarrow \pm\infty$. In other words, in order to have solutions that stay bounded with the passing of time (also known as stable solutions), α must be zero. On the other hand, given that $\alpha = 0$, if β is an integer, the general solution to the equation will have to be a combination of a periodic function and a second solution that grows linearly as $\xi \rightarrow \infty$, which also means that the solution is unstable. Consequently, the only way to obtain stable solutions and thus achieve confinement of the particle in one dimension is to set α to zero and let β be a real number that is not an integer.

The fact that β cannot be an integer gives rise to regions of stability and instability in a-q space. Being a non-integer real number simply means that, in an arbitrary dimension, β is the sum of an integer and some number β_i that ranges from zero to one. $\beta_i = 1$ or 0 , therefore, is the boundary condition that separates the stable solutions from the unstable ones; all we need now is to obtain a function that relate a_i and q_i to β_i . Fortunately, substituting the Fourier series of the Floquet solution [4],

$$u(\xi) = \sum_{n=-\infty}^{\infty} c_{2n} e^{i(\beta_i + 2n)\xi},$$

back into Mathieu's equation gives

$$q_i c_{2n+2} - (a_i - (\beta_i + 2n)^2) c_{2n} + q_i c_{2n-2} = 0. \quad (2.6)$$

Equation 2.6 is the last theoretical link to determining the boundaries of the stability regions. By setting β_i to zero and one, we can obtain a series of a'_i 's as functions of q_i for $n = 0, 1, 2, 3, \dots$. These functions divide a-q space into regions of stability and instability (Figure 2.2).

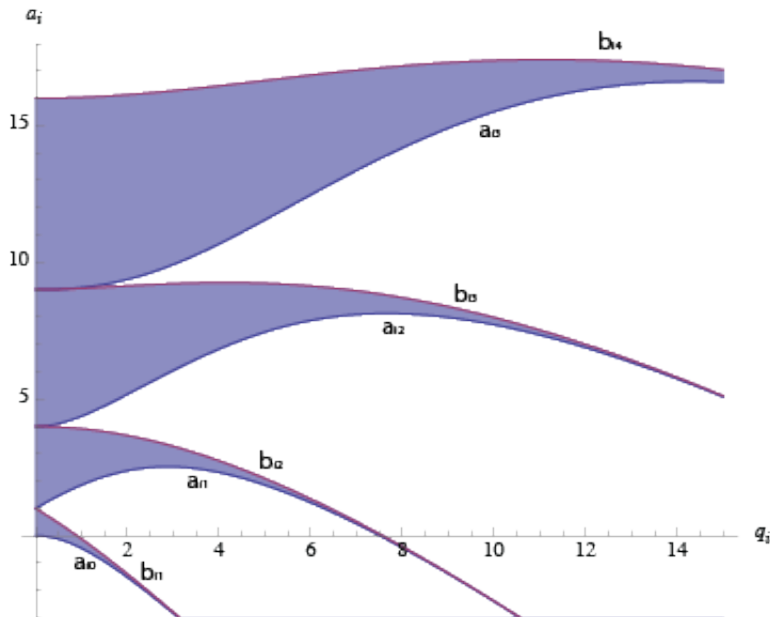


Figure 2.2: Stability regions (shaded) in an arbitrary dimension. The boundaries of these regions are functions of a_i in terms q_i . Setting β_i to 0 gives $a_{i,2n}$ and $b_{i,2n+2}$ while setting β_i to 1 gives $a_{i,2n+1}$ and $b_{i,2n+1}$.

Finally, in order to produce confinement in both x- and y-dimensions, the set of required values for (a_i, q_i) must make up the region where the stability regions in the x-dimension overlap with those in the y-dimension. Finding the second set of stability regions in another dimension is easy after we have done so for an arbitrary dimension; since $a_x = a_y$ while $q_x = -q_y$, the stability regions for y are symmetric to those for x about the q-axis. For the purpose of constructing a linear Paul trap, we are only interested in the region where

both a_i and q_i are smaller than one [2]; Figure 2.3 shows the region of interest.

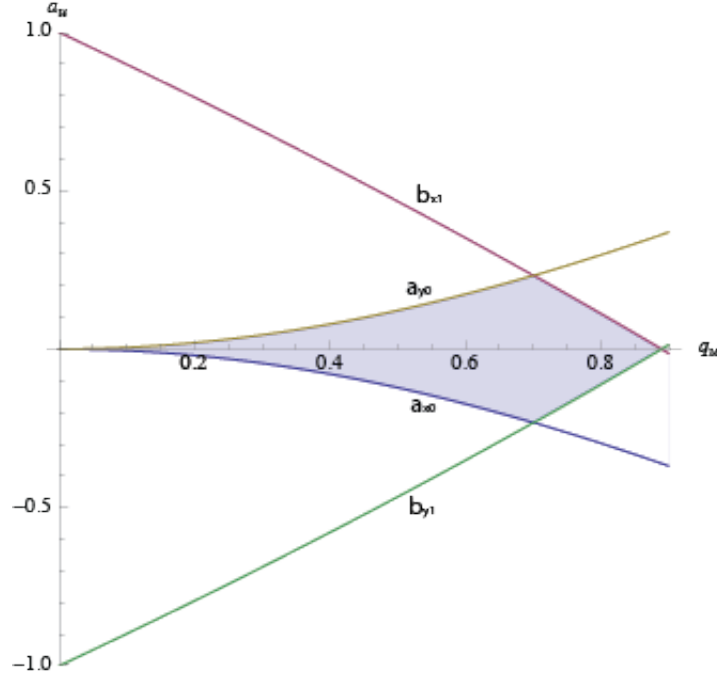


Figure 2.3: The stability region of interest for confinement in both x- and y-dimensions

In short, only combinations of (a_i, q_i) that are within the shaded region can lead to confinement of the particle on both x and y-axes. As a_i and q_i are themselves related to physical properties of the trap, such as its geometry and the RF potential, by equation 2.5, they are crucial parameters to consider during the actual design and engineering of the trap. Typically, traps are built such that $a < q^2 \ll 1$ to ensure tighter confinement.

That being said, since the parameters a_i and q_i are themselves mathematical constructions, it is difficult to immediately visualize how a particular choice of (a_i, q_i) dictates the physical properties of the trap and its ability to trap a certain particle. The following section offers alternative ways to model condi-

tions leading to confinement of the particles. These more intuitive descriptions of confinement conditions eventually provide valuable design considerations for building a physical trap.

2.2 Design Considerations

When it comes to designing an actual trap for an experiment, we already know the masses and charge of the particles we want to trap. In fact, as mentioned in Chapter 1, we have chosen to trap ${}^9\text{Be}^+$ and a diatomic molecular ion with very specific purposes in mind. Therefore, the first criterion for choosing the physical parameters of the trap is that they should enable it to confine both mass-charge combinations. In order to aid the process of selecting those physical parameters, the stability region in Figure 2.3 is first transformed into mass-charge (m-Q) space to represent a range of charge and mass combinations that an imaginary ideal linear Paul trap can confine.

2.2.1 Stability in m-Q space

Similar to defining the stability region in a-q space, we need to find functions of m in terms of Q at the boundary condition $\beta_i = 0$ or 1 . In the limit of $q_x^2 \ll 1$,² expanding from equation 2.6, the leading terms of the power series, up to second order [4], for the two boundaries in Figure 2.3, a_{x0} and b_{x1} , are

$$a_{x0}(q_x) = -\frac{1}{2}q_x^2 \quad (2.7)$$

²In most real linear Paul traps, q_x^2 is much smaller than 1 so as to minimize the micro-motion of the trapped ion [2]. See Section 2.2.2 for more details.

and

$$b_{x1}(q_x) = 1 - q_x - \frac{1}{8}q_x^2. \quad (2.8)$$

From equation 2.5, we have a_x in terms of q_x

$$a_x = \frac{2U_0r_0^2}{V_0z_0^2}q_x \quad (2.9)$$

and m as a function of Q

$$m(Q) = -\frac{2V_0}{\Omega^2r_0^2q_x}Q. \quad (2.10)$$

If we replace the left-hand side in equations 2.7 and 2.8 with equation 2.9, we can solve for q_x in terms of r_0 , z_0 , U_0 , V_0 and Ω . In other words, given the geometry of the trap, the RF and DC inputs, we can find $m(Q)$ at $\beta = 0$ and $\beta = 1$ by solving for q_x in equations 2.7 and 2.8. Since equations 2.7 and 2.8 are both quadratic, there will be four solutions for q_x , providing four functions of m in terms of Q from equation 2.10. These functions, plotted in m-Q space in Figure 2.4, are the boundaries (one of the boundaries is the vertical axis for $q_x = 0$) for the stability regions in the x-dimension. By superimposing the same plot for the y-dimension, the overlap of the two plot (shaded in Figure 2.4) gives the set of mass-charge combinations that a trap with a particular geometry, RF and DC potentials is able to confine.

A plot such as the one in Figure 2.4 comes in really handy when one wants to define the trapping capacity of a specific trap, i.e. the combinations of mass and charge it can actually trap. For instance, a vertical line in Figure 2.4 cuts

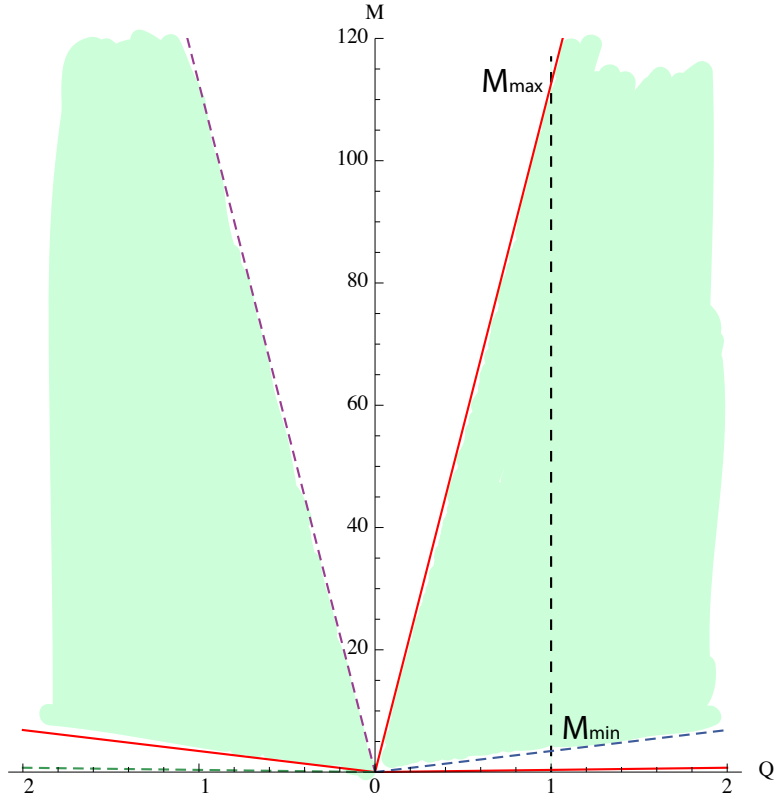


Figure 2.4: The stability region in m - Q space for confinement in both x - and y -dimensions, plotted for $r_0 = 1.25$ mm, $z_0 = 1.5$ mm, $V_0 = 100$ V, $U_0 = 1$ V, and $\Omega = 10$ MHz (this is the configuration for the trap we have designed). The two shaded regions represent the set of mass and charge combinations this particular trap can confine. The vertical line intersect the boundaries of one of the shaded regions at $m = 3.44$ u and $m = 113$ u, which give the trapping capacity of the trap, i.e. the range of singly charged masses it can confine.

though one shaded region of stability at one unit charge. Its two intersections with the two boundaries give the maximum and minimum masses that the trap is capable of stabilizing, given that the ion is singly charged; anything lighter or heavier will simply fall out of the trap according to this model. Table 2.1 lists the trapping capacities of three hypothetical traps at different RF and DC inputs.

Trap	Geometric parameters	V_0, U_0, Ω	Trap Capacity	(a_x, q_x)
A	$r_0 = 0.1$ mm $z_0 = 0.1$ mm	$V_0 = 250$ V $U_0 = 10$ V $\Omega = 150$ MHz	$M_{min} = 5.65$ u $M_{max} = 33.9$ u	$(0.018, -0.23)$ for $^{24}\text{Mg}^+$
B	$r_0 = 0.769$ mm $z_0 = 1.25$ mm	$V_0 = 400$ V $U_0 = 10$ V $\Omega = 12.7$ MHz	$M_{min} = 22.4$ u $M_{max} = 541.4$ u	$(0.00019, -0.10)$ for $^{199}\text{Hg}^+$
C	$r_0 = 1.25$ mm $z_0 = 1.50$ mm	$V_0 = 100$ V $U_0 = 1$ V $\Omega = 10$ MHz	$M_{min} = 3.44$ u $M_{max} = 113$ u	$(0.0048, -0.35)$ for $^9\text{Be}^+$

Table 2.1: This table summarizes the trapping capacities of three hypothetical traps at three different sets of DC and RF potentials. Here u is the atomic mass unit. Traps A and B are model after those used in [5] and [6] respectively and trap C is our own trap. The values of (a_x, q_x) are calculated for the ions that those trap were designed to confine, in order to show that they all function well within the approximation we have used to derive Figure 2.4. This table serves to verify our understanding of the theory and also demonstrates that more than one trap design will enable us to trap co-trap $^9\text{Be}^+$ and a diatomic ion that is not too much heavier than it.

It is apparent from table 2.1 that more than one trap design will enable us to co-trap $^9\text{Be}^+$ and a diatomic ion that is not too much heavier than it³. But we also have other considerations that limit the choices of trap parameters. The angular frequencies of oscillations of the trapped ion as well as the “potential depth” or “pseudopotential” in which it is confined are crucial aspects of the trap’s physical properties. In conjunction with the m-Q stability region, we therefore also need to examine our requirements for trap frequencies and potential depths and take them into consideration.

³ O_2^+ is a possible candidate as a co-trapped ion. See 4.3 for details on the choice molecular ion to be co-trapped.

2.2.2 Pseudopotentials and Trap Frequencies

The pseudopotential model is one in which we approximate the time-dependent potential generated by the trap electrodes to one that is time-independent and quadratic, similar to that of a harmonic oscillator. With this model, we can easily obtain the angular frequencies at which a single trapped ion is oscillating in both the radial (the xy-plane) and axial (the z-axis) directions.

This approximation is only valid under the assumption that Ω is sufficiently large in the limit of $a_i, q_i^2 \ll 1$. Under this assumption, the motion of the trapped ion projected into the radial or the axial direction is a secular motion at a frequency much lower than Ω , superimposed with driven excursions at the much higher RF frequency of Ω . Since the amplitude of the driven excursions are a factor of $\frac{q_i}{2}$ smaller than that of the secular motion, the driven excursions are known as the micromotion. In most cases, the micromotion is negligible due to its high frequency and small amplitude; the trajectory of the trapped ion is therefore approximated to the secular motion [3].

Consequently, considering only the RF potential applied to the rod electrodes, mass m with charge Q moves in an effectively harmonic pseudopotential⁴

$$\Phi = \frac{QV_0^2}{4m\Omega^2 r_0^4}(x^2 + y^2) = \frac{m}{2Q}\omega_r^2(x^2 + y^2) \quad (2.11)$$

where

$$\omega_r = \frac{QV_0}{\sqrt{2}m\Omega r_0^2}. \quad (2.12)$$

⁴The equations given here assume that the electrodes used for the trap are ideal. A geometric factor can be incorporated in these equations to correct for the “non-idealness” of the potential. See Section 2.4.

Similarly, in the z- or axial direction, the potential (not a pseudopotential as we can see that equation 2.2 already fits the bill without any approximation) created by the static DC potential applied to the endcap electrodes is

$$\phi_s = \frac{m}{2Q}\omega_z^2[z^2 - \frac{1}{2}(x^2 + y^2)] \quad (2.13)$$

where

$$\omega_z = \sqrt{\frac{2QU_0}{mz_0^2}}. \quad (2.14)$$

The addition of the static pseudopotential weakens the pseudopotential generated by the rod electrodes in the radial plane so that it becomes

$$\phi_r = \frac{m}{2Q}(\omega_r^2 - \frac{1}{2}\omega_z^2)(x^2 + y^2). \quad (2.15)$$

In other words, the angular frequency in the radial direction is actually

$$\omega'_r = \sqrt{\omega_r^2 - \frac{1}{2}\omega_z^2}. \quad (2.16)$$

For all practical purposes, equations 2.16 and 2.14 give the angular frequencies of oscillations in the radial and axial directions respectively and define the motions of trapped ions.

Using equation 2.15 and 2.13, we can also estimate the potential depth, i.e. the potential difference between the center of the trap and the edge of the trap. Here we define the edge of the trap as just outside the surface of the electrodes. As a result, in the radial direction potential depth is just the

difference between ϕ_r at $(0, 0)$ and that at, say, $(0, r_0)$, which is

$$D_r = \frac{QV_0^2}{4m\Omega^2 r_0^2} - \frac{U_0 r_0^2}{2z_0^2}. \quad (2.17)$$

Similarly, it is not difficult to derive from equation 2.13 or just argue intuitively that the potential depth in the axial direction is U_0 .

After establishing the pseudopotential approximation, we now have all the theoretical constructions needed to make a summary of the conditions, besides that it should be able to confine ${}^9\text{Be}^+$ and another diatomic molecular ion not too much heavier than ${}^9\text{Be}^+$, that have to be met by the geometric and electrical parameters of the trap.

- Ω must be large so that the magnitudes of q_x and q_y are small enough for the pseudopotential approximation to be valid.
- Since the secular frequencies determines the time constants at which any external agent interact with the trapped ion, they set the upper limit of the precision at which measurements can be made. Also, electronic noise scales $1/f$. Hence, in general, we need to maximize these frequencies.
- The potential depth needs to be large as a deeper pseudopotential well usually corresponds to a “tighter” trap that is less likely to lose the ion. That means, from 2.17, r_0 and Ω (hence the kinetic energy of the trapped ion) need to be relatively small while V_0 needs to be relatively large. Additionally, U_0 cannot be a large voltage compared to V_0 if r_0 and z_0 are similar in their order of magnitude.

- Finally, from a more practical perspective, r_0 and z_0 cannot be so small that they cannot be machined with high precision by available methods of fabrication. We should also design the geometry of the trap electrodes to allow as much optical control as possible.

The points listed in the summary above essentially demonstrate why it is important to consider the pseudopotential approximation of the ideal Paul trap although the solution to the Mathieu equation provides sufficient conditions for achieving confinement of the ions. For instance, there is a qualitative set of upper and lower limits for Ω . It needs to be large enough for the pseudopotential approximation to be valid; but it cannot not be too large as a very large Ω will result in a high kinetic energy for the trapped ion and a corresponding need for a high RF potential in order to trap the ions in a deep pseudopotential well. A similar argument also applies to U_0 —it cannot be so large that it significantly compromises the radial trapping frequency and potential depth while it has to be large enough to provide secure axial confinement. With all these considerations in mind, for trapping ${}^9\text{Be}^+$ we have calculated the trap frequencies and radial potential depths for two of the same virtual traps in table 2.1 and the results are presented in table 2.2.

Essentially, the numbers in table 2.2 demonstrate some of the trade-offs we need to consider when designing the trap. In general, smaller traps tend to have higher trapping frequencies and radial potential depths for the same electrical inputs; but they may require more sophisticated fabrication techniques or tools that are not readily available. On the other hand, for the same trap, having a lower the RF frequency means that the same trap frequencies and

V_0, U_0, Ω	Trap B	Trap C
$V_0 = 200 \text{ V}$ $U_0 = 1 \text{ V}$ $\Omega = 20 \text{ MHz}$	$\nu_z = 0.589 \text{ MHz}$ $\nu'_r = 3.24 \text{ MHz}$ $D_r = 22.6 \text{ V}$	$\nu_z = 0.491 \text{ MHz}$ $\nu'_r = 1.21 \text{ MHz}$ $D_r = 4.00 \text{ V}$
$V_0 = 500 \text{ V}$ $U_0 = 5 \text{ V}$ $\Omega = 20 \text{ MHz}$	-	$\nu_z = 1.10 \text{ MHz}$ $\nu'_r = 3.04 \text{ MHz}$ $D_r = 25.4 \text{ V}$
$V_0 = 100 \text{ V}$ $U_0 = 1 \text{ V}$ $\Omega = 10 \text{ MHz}$	-	$\nu_z = 0.491 \text{ MHz}$ $\nu'_r = 1.21 \text{ MHz}$ $D_r = 4.00 \text{ V}$

Table 2.2: This table summarizes the trapping frequencies (reported in Hz and thus the symbol ν is used) and the radial potential depths of two hypothetical traps for a ${}^9\text{Be}^+$ ion at three different sets of DC and RF potentials. For trap B, $r_0 = 0.769 \text{ mm}$ and $z_0 = 1.25 \text{ mm}$. Similarly for trap C, $r_0 = 1.25 \text{ mm}$, $z_0 = 1.5 \text{ mm}$. For two of the three combinations of DC and RF potentials, Trap B is unable to confine ${}^9\text{Be}^+$. Calculations are not done for Trap A because it was designed for RF signals with much higher frequencies.

potential depth can be achieved with a lower peak-to-peak voltage, although it also further compromises the pseudopotential approximation. Finally, for the same RF frequency and trap geometry, a higher V_0 is always more desirably provided that we can build a RF resonator that has a sufficiently high Q factor (see Section 3.2 for details). In short, we have now considered the ability of the trap to confine certain mass-charge combinations as well as all the players in the pseudopotential approximation; we are now ready to pinpoint a particular design to suit our purpose for co-trapping ${}^9\text{Be}^+$ with another molecular ion.

2.3 Construction of the Trap

Like the ideal Paul trap in Figure 2.1, our design of the trap consists of four electrodes, machined out of oxygen-free high conductivity (OFHC) copper,

around the z -axis of the trap as shown in Figure 2.5(a) (drawings of the final machined design are in Appendix A). But unlike the ideal trap, the electrodes do not have hyperbolic surfaces and the endcap electrodes are replaced by two of the electrodes not adjacent to each other being segmented in to five sections. The segmented electrodes have only DC voltages applied to them, dividing the center of the trap into two trapping regions (the three regions in between electrode pairs 2 and 4) in which the ions can sit and providing a gradient of DC voltages that supply the axial confinement of ions⁵. The unsegmented electrodes have only the RF voltage applied to them. Held together by insulating parts made of Macor, the four electrodes generate a potential that approximates that of an ideal Paul trap.

From the discussion in Section 2.2, we can surmise that generally smaller traps gives a tighter confinement, holding other conditions constant. Given that the tolerance our fabrication method can achieve here at the College is about one thousandth of an inch and our allowance of machining error about 2%, the smallest r_0 and z_0 ⁶ that we can confidently machine are in the order of millimeters. Therefore, we have chosen r_0 to be 1.25 mm and z_0 to be 1.5 mm, which makes the trap easy enough to machine while also robust to drifts in RF voltage applied to the RF electrodes (more on this subject later).

All electrodes are shaped like blades (Figure 2.5(b) and (c)), with the edges closest to the trap center tapered down to rounded tips with radius of

⁵With this DC electrode assembly, we can adjust the potential of each electrode individually. A highest-middle-low-middle-highest potential configuration will give us a single potential well for confinement. A high-low-high-low-high potential configuration will give us a double-well.

⁶ r_0 is now defined as the perpendicular distance from the tip of the electrode to the z -axis of the trap. z_0 is half the width of electrodes 2, 3, and 4, as indicated in Figure 2.5(b).

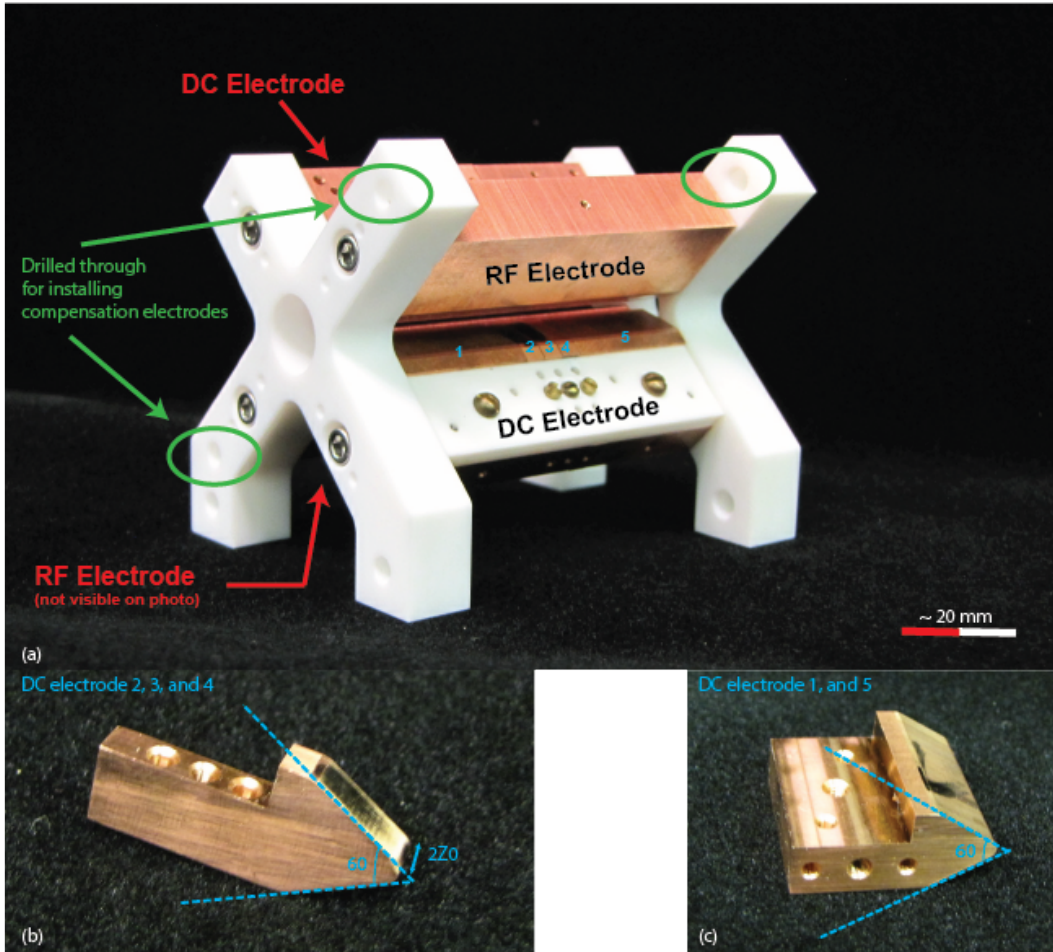


Figure 2.5: The assembly of electrodes of the actual linear Paul trap we have machined.

curvature r_t (similarly shaped electrodes are also used in [7]). Although the electrodes do not have hyperbolic surfaces, r_t is carefully chosen to match the radius of curvature of the equipotential surface at the electrode. We have also calculated that the angle θ needs to be 60 degrees to allow maximum solid angle for optical access given other physical parameters of the electrodes. We have chosen this particular shape for the electrodes for the ease of machining and assembling while keeping the shape of the electrodes approximate to that

of an ideal trap, at least from the trapped ions' perspective.

The assembly of electrodes shown in Figure 2.5 provide the oscillating field for confining the ions in the radial direction and a DC gradient in the axial direction. We also plan to use the the pre-drilled holes on the Macor end pieces (see Figure 2.5(a)) for compensation electrodes that will provide two additional degrees of freedom to “nudge” the ions around in the trap. Those electrodes will look similar to those in [7] and will have DC voltages applied to them, which can be adjusted to shift the location of minimum potential and ensure that it coincides with the geometric center of the trap. In this way, the compensation electrodes and the segmented DC electrodes together provide three independent axes in which a trapped ion can be centered using a DC potential.

With easily accessible DC voltage, RF voltage and frequency, the geometry of our trap should allow robust co-trapping of ${}^9\text{Be}^+$ with another diatomic molecule in the same potential well. For instance, if the applied RF signal has peak-to-peak voltage 100 V and frequency 10 MHz while the DC voltage applied to electrodes 2 and 4 exceeds that of electrode 3 by 1 V, we can confine both ${}^9\text{Be}^+$ and ${}^{16}\text{O}^+$, a potential candidate for our diatomic molecular ion. Their (a_x, q_x) values will be $(0.0048, -0.35)$ and $(0.0027, 0.20)$ respectively, both of which fall within the pseudopotential approximation. For ${}^9\text{Be}^+$, the radial and axial trapping frequencies will be about 1.21 MHz and 0.491 MHz respectively; the radio potential depth is about 8 V. Our design of electrodes are robust enough that moderate drifting in the RF voltage and frequency applied to the electrodes will not result in loss of trapped ions or breaking

down of the pseudopotential approximation. Therefore, the RF signal we need to reliably stabilize ${}^9\text{Be}^+$ and another diatomic ion not too much heavier does not have stringent or unrealistic requirements for the power supplies for the electrodes.

Finally, we have also designed our trap to be ultrahigh vacuum compatible. The materials used for construction are chosen to minimize surface and bulk outgassing while the parts are all engineered to prevent virtual leaks in the vacuum chamber. More details on procedures and precautions for creating UHV will be presented later in Section 3.3.

Notably, there is an inherent asymmetry in producing the DC electric field in our trap. The static potential that provides axial confinement is only applied to two segmented electrodes. As a result, the actual trap frequencies are in general slightly different from the calculated values above. Fortunately, instead of tossing the theoretical model we have just described out of the window, we can make one modification to it to make model's prediction reasonably consistent with reality. Before ending this chapter on the linear Paul trap, we would like to present this theoretical modification; although it is non-essential to our purpose of building a functional trap, it is nonetheless something interesting we may want to characterize once the entire trap system has been completed.

2.4 Final Thought: The Geometric Constant

While the RF potential applied to the electrodes produces an electric field described by equation 2.1 near the center of the trap, the same in cannot be necessarily said for the DC potential. Here, we need to introduce to the potential produced by the “endcap electrodes” Φ_{end} the geometric constant κ , a correction factor that accounts, in our case, for the asymmetry in the geometry of our real trap. In other cases, when the geometry of the trap is symmetric, as we will see later in this section, we may still need κ to account for the complicated geometry of conductors involved in determining the field produced by the endcap electrodes along the trap axis [6]. Numerically, κ ranges from zero to one. Near the center of the trap, which is also the origin of the coordinate system in our model, the potential produced by the endcap electrodes become

$$\Phi_{end} = \frac{U_0}{z_0^2} \kappa [z^2 - \frac{1}{2}(x^2 + y^2)]. \quad (2.18)$$

Consequently, the trap frequencies, ω_z and ω'_r , become

$$\omega_z = \sqrt{\frac{2\kappa QU_0}{mz_0^2}} \quad (2.19)$$

and

$$\omega'_r = \sqrt{\frac{Q^2 V_0^2}{2m^2 \Omega^2 r_0^4} - \frac{\kappa QU_0}{mz_0^2}}. \quad (2.20)$$

There are more than one way to obtain a numerical value for κ . Some ion trapping groups have calculated κ numerically with computer simulations. For instance, in [8], κ has been numerically determined to be 0.325. Direct

calculation of κ from the geometry of our trap is cumbersome. It would be, however, interesting and useful to numerically simulate the field produced by our electrodes and obtain κ . We can also measure the trap frequencies of ions in the trap once the entire system is constructed and functional. Fitting those frequency data to equations 2.19 and 2.20 will also give us κ and also determine how well our theoretical model actually describes the behavior of a real trap.

Modelling the electric field produced by the endcap electrodes are less complicated although still difficult if the arrangement of electrodes is symmetric. Here, we present a plausible approach for a real linear Paul consisting of four thin segmented rod electrodes. Although this geometry is not the same as our own, the model sheds some light on how the geometry of a real trap determines the deviation of the trapped ion's behavior from that in an ideal trap.

Suppose the electrode geometry of a real trap consists of four thin linear segmented conductors set parallel and equally spaced around the z-axis, and at equal distance r_0 from it, as shown in Figure 2.5. The endcap electrodes in this case are the four outer segments where the DC potential U_0 is applied. The RF potential is applied to the inner segments. Consequently, the length of the inner segments is $2z_0$ in order to be consistent with the established theoretical model. We need to introduce one more variable, the distance z_c from the center of the trap to one end of the electrode assembly, in this modified model in order to fully account for the geometry of the real trap⁷. z_c is assumed to be much larger than z_0 and r_0 .

⁷In our model for the ideal trap, z_c is effectively infinite.

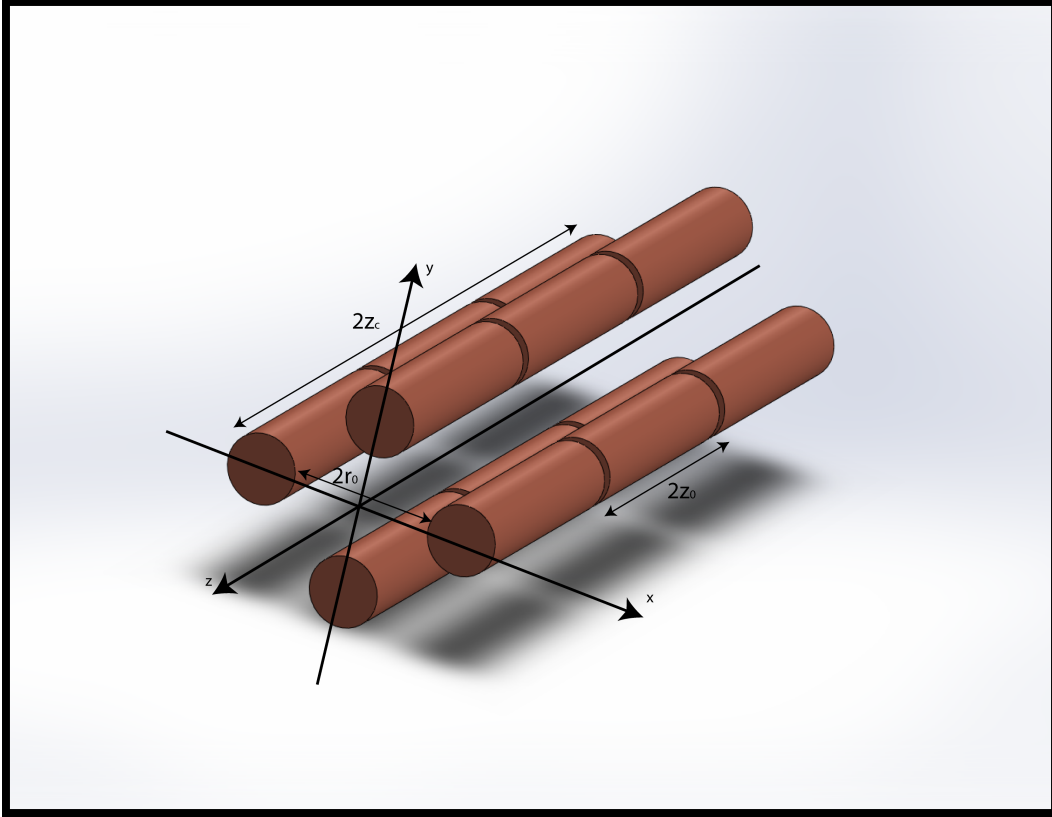


Figure 2.6: Cartoon of a real trap that consists of four thin linear segmented conductors set parallel and equally spaced around the z -axis, and at equal distance r_0 from it. The endcap electrodes in this case are the four outer segments where the DC potential U_0 is applied. The RF potential is applied to the inner segments.

The potential generated by the endcaps, which are the outer segments of the electrodes in this case, is an approximate solution to the boundary value problem by assuming the conductors to be narrow strips, circular arcs in cross-section, centered on the z -axis [2]. The boundary conditions for the endcap electrodes in standard cylindrical coordinates are as follows: for $-z_c < z < -z_0$ and $z_0 < z < z_c$ the potential is U_0 at $r = r_0$ and $0 < \theta < \delta\theta, \pi/2 < \theta < (\pi/2 + \delta\theta), \pi < \theta < (\pi + \delta\theta)$, and $3\pi/2 < \theta < (3\pi/2 + \delta\theta)$, where $\delta\theta \ll \pi$.

Given these boundary conditions, the solutions for the potential generated by the endcap electrodes is

$$\Phi_{end} = \sum_{n,m=0}^{\infty} A_{nm} I_m(n\pi r/z_c) \cos(n\pi z/z_c) \cos(m\theta) \quad (2.21)$$

where $I_m(x)$ is the modified Bessel function of the first kind,

$$A_{nm} = \frac{4U_0}{\pi^2 nm} \frac{\sin(n\frac{z_0}{z_c}\pi)}{I_m(\frac{n\pi}{z_c}r_0)} [1 + \cos(m\pi) + 2\cos(\frac{m\pi}{2})] \sin(\frac{m\delta\theta}{2})$$

for $n, m = 1, 2, 3\dots$ and

$$A_{n0} = -\frac{8U_0}{\pi n} \frac{\sin(n\frac{z_0}{z_c}\pi)}{I_0(\frac{n\pi}{z_c}r_0)} \frac{\delta\theta}{\pi}.$$

If we expand the Bessel functions in equation 2.21 within the vicinity of the origin, where $r \approx 0$, and assume that all terms involving higher than second order powers of $\frac{r}{z_c}$ are negligible, we can simplify equation 2.21 to

$$\Phi_{dc} = \sum_{n=0}^{\infty} A_{n0} - \frac{U_0 r^2}{2z_0^2} \sum_{n=0}^{\infty} 4n \frac{z_0^2}{z_c^2} \frac{\sin(n\frac{z_0}{z_c}\pi)}{I(\frac{n\pi}{z_c}r_0)} \delta\theta. \quad (2.22)$$

Note that $x^2 + y^2 = r^2$ and compare equation 2.22 with equation 2.18, we can conclude that κ is the series

$$\kappa = \sum_{n=0}^{\infty} 4n \frac{z_0^2}{z_c^2} \frac{\sin(n\frac{z_0}{z_c}\pi)}{I(\frac{n\pi}{z_c}r_0)} \delta\theta. \quad (2.23)$$

In equation 2.23, κ is derived by considering the boundary conditions of trap with symmetric electrodes. In theory, we can do the same boundary

condition problem for our trap, which has asymmetric electrodes. For the purpose of constructing a functional trap, however, we do not think it necessary to obtain an exact numerical value for κ as it is usually in the order of 10^{-1} and therefore does not significantly affect the trapping capacity or frequencies. Our theoretical exploration of κ stops here also due to the ambiguity in the definition of $\delta\theta$ in the literature. As mentioned earlier, it may prove to be instructive to numerically simulate the electric field produced by our electrodes or calculate κ from actual trap frequency data.

The linear Paul trap electrodes we have constructed is central to the system of apparatus that will house our proposed experiment. In this chapter, we have outlined the theory of trapping ions with an oscillating electric field, discussed important considerations for designing the trap and described the actual trap we have constructed. The next logical step is therefore to think about the rest of the system that will supply the RF and DC signals to the trap electrodes, create the ultra-high vacuum environment essential to our experiment, and image the trapped ions.

Chapter 3

Putting it All Together: the Rest of the Paul Trap System

Chapter 2 takes us about half way through the apparatus-building phase of this thesis. To complete the rest of our journey towards measuring the time variation of μ , we need to create the environment for high-precision frequency metrology. Therefore, the remaining challenges include constructing the power supplies that provide the desired DC and RF signals, generating the ultra-high vacuum (UHV) environment, and completing an imaging system so that we can observe the trapped ions. This chapter will take us down the first few miles of this treacherous remainder of our journey by providing some preliminary designs, thoughts and questions

3.1 Overview

Figure 3.1 includes a schematic of the entire Paul trap system and Appendix C an inventory of commercially available as well as “home-made” parts. The trap will be housed in a spherical-octagonal vacuum chamber¹, which has eight 2.75” ConFlat (CF) ports on its sides and two 8.00” ones on the top and bottom. Six of the 2.75” ports and the top 8.00” port will be fitted with fused-silica windows² and used for optical access and imaging of the trapped ions. Meanwhile, the other two 2.75” ports will connect to the RF power supply via an RF vacuum feedthrough³ and UHV instruments respectively. Finally, the bottom 8.00” port will be fitted with a CF flange with a welded-in multi-pin feedthrough⁴; the flange will provide the base onto which we can attach the ion trap and the multi-pin feedthrough will provide connections to the DC power supply.

We can divide the system described above into three subsystems: the power supplies for the electrodes, the UHV system, and the imaging system. The following sections will address these subsystems separately and present what we already know about them.

¹Kimball Physics, MCF800-SphOct-G2C8

²The top viewport can be anti-reflection (AR) coated for 313nm. The smaller viewports on the sides of the spherical octagon can also be AR coated according to the wavelengths of lasers we are going to use. Kurt J. Lesker, Kimball Physics, Nor-Cal Products, and Thorlabs are some suppliers to consider for CF viewports.

³Kurt J. Lesker, FTT1023253

⁴Kurt J. Lesker, IFDGG501056B

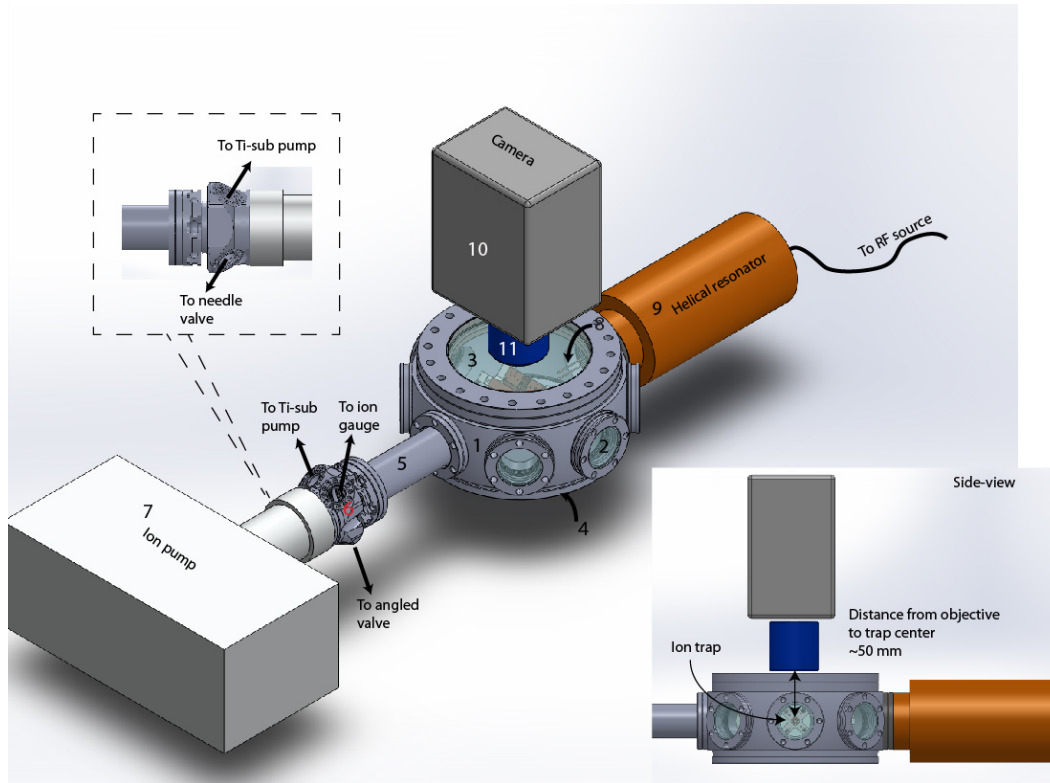


Figure 3.1: A schematic of the Paul trap system, including the main vacuum chamber, power supplies for the trap electrodes, the UHV pumping system and the imaging system.

3.2 Generating the Trapping Potential

In order to generate the trapping potential described in Chapter 2, we need to build both the DC and the RF supplies for our electrodes (Figure 3.2). Since our entire vacuum system will go through a bake-out process (see Section 4.3), electrical connections inside the vacuum chamber cannot be soft-soldered. Therefore, we have made threaded holes at the back of the DC electrodes for securing copper wires to the them to make electrical contact. The bolts that hold the Macor pieces and the RF electrodes together can also serve as

points of electrical contact. There are also commercially available in-vacuum connectors⁵. As shown in Figure 3.2, the RF components will include an RF generator, a directional coupler, an amplifier and a helical resonator. The DC signals will be computer-controlled⁶ and will pass through one or two low-pass filters before reaching the electrodes. This section provides essentially a complete “recipe” for building the helical resonator required for generating the RF signal; it will also include a discussion on filtering the DC signals as well.

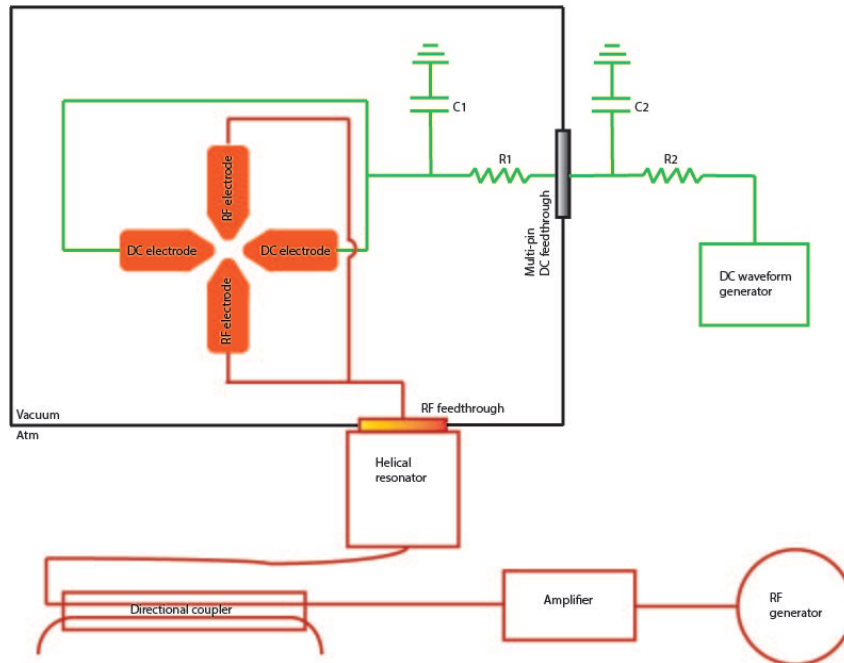


Figure 3.2: A schematic of the DC and RF power supplies of the system and how they are wired to the trap electrodes.

⁵Kurt J. Lesker has such accessories for multi-pin feedthroughs

⁶National Instrument, PXI-6733 or the NIST-design fast-update digital-to-analog converter used in [9].

3.2.1 RF Power Supply

In Chapter 2, we have determined that an RF potential with frequency 10 MHz and peak-to-peak voltage 100 V should enable our trap to confine both ${}^9\text{Be}^+$ and a diatomic ion not much heavier than it, such as ${}^{16}\text{O}_2^+$. To generate this potential across one pair of trap electrodes, we need to “home-make” a helical resonator. There are three advantages for using a resonator instead of connecting an RF source directly to the trap. First, the resonator allows impedance matching between the load, namely the ion trap, and the source, therefore maximizes the power transferred to the load. Second, a resonator also acts like a transformer and boosts voltage at the trap. Finally, the resonator forms an RLC circuit with the ion trap, which effectively acts like a band-pass filter, passing a range of frequencies centered on a resonance while attenuating those lower or higher than the range. We essentially want our resonator to be a high quality factor (high-Q) band-pass filter with a narrow bandwidth so as to reduce noise injected into the system and concentrate the power from the RF source on the resonance frequency we need to trap ions.

This section and Appendix B⁷ together can be read as a “cookbook” for obtaining the geometric parameters that will determine the resonance frequency and maximizes the quality factor Q. We have adopted our circuit model of the resonator from [10]⁸.

⁷Appendix B provides the codes of a Mathematica notebook that will perform all the calculations needed to obtain the physical parameters of the resonator, as shown in Figure 3.3. It comes with step-by-step instructions on how to design the resonator.

⁸Our replication of the calculations and Figures 10, 15, and 16 in [10], although matching in terms of trend to the originals, is not exactly identical to them. This is because certain assumptions made in [10] are unclear. For instance, it is not clear in the article what the exact relationship between B, b, and D is. The article also does not state explicitly how the

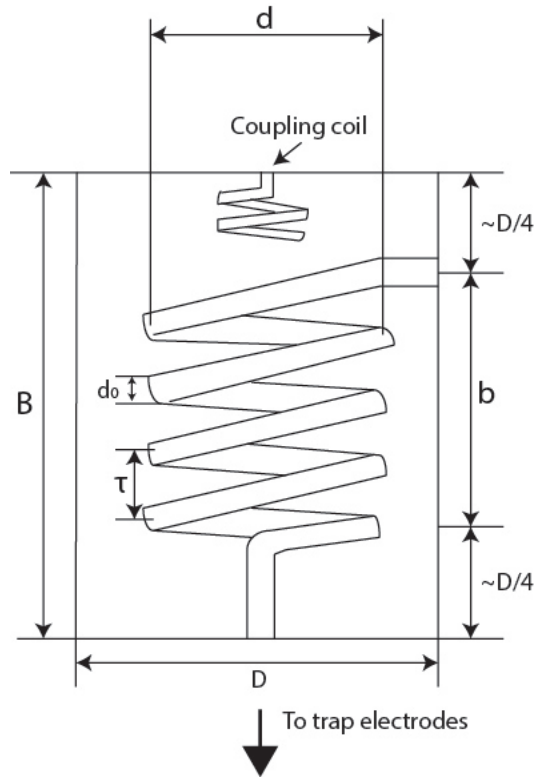


Figure 3.3: A schematic diagram of the helical resonator. The resonator coils and shield are made of copper. The shield is grounded.

The resonator will contain two coils, a main coil and a smaller one to couple the RF signal into the main coil, both of which are made of copper wires and enclosed in a copper shield (Figure 3.3). The circuit model essentially reduces the system of the resonator and the RF trap electrodes to an RCL circuit and allows us to choose a combination of $(d/D, d)$ that maximizes Q , given the trap capacitance and resistance, which we can measure directly, the resonance frequency we need, the diameter of the wire used (typically 5 mm), and the

group calculated the length of the wire used for the main coil from d and τ . Since more time than necessary has already been spent on trying to get these calculations to match, the most logical way to proceed now is to construct the resonator using the calculated geometrical parameters as guidelines, use it to generate an RF signal and adjust the geometry of the coils, literally by stretching or squishing them.

winding pitch τ of the mail coil (typically twice the diameter of the wire). Given a geometry of the main coil that maximizes Q , we can then manipulate the geometry of the smaller coil to match the input impedance of the resonator with that of the RF source, which is typically 50Ω . The final product is a resonator that has the correct resonance frequency, with a large Q , and a matched input impedance with the source. All calculations described above can be done using the Mathematica notebook in Appendix B.

For demonstrating how the calculations work, we have calculated some of the geometric parameters of a resonator with resonance frequency 10 MHz (Table 3.1). It is to be used with a hypothetical trap with capacitance 15 pF and resistance 5Ω . We have assumed that the diameters of the copper wires used for both coils to be 5 mm and 3.5 mm respectively while the winding pitches is twice the diameter for each coil. These numbers are some of the initial inputs in Appendix B, which is meant to be read together with this section and [10]. The Q of this resonator is about 185.

Diameter of main coil (d)	7.0 cm
Height of main coil (b)	22.8 cm
Diameter of shield (D)	17.5 cm
Height of shield (B)	31.5 cm
Diameter of coupling coil (d_a) (The coupling coil has 3 turns)	4.3 cm

Table 3.1: Parameters of a resonator that will generate a 10 MHz resonance frequency, impedance-matched to a 50Ω RF source. See Appendix B for details on calculations.

Once constructed, we can connect the helical resonator to the trap via an RF vacuum feedthrough, with the resonator outside the vacuum chamber.

The directional coupler (Figure 3.2) will allow us to monitor the percentage of power that actually goes into the trap electrodes from the RF source; we can adjust the geometry of the smaller coil by simply stretching or squishing it, to maximize this percentage. With an appropriate amplifier⁹ and a standard, commercially available RF generator, we should have a functioning high-Q RF supply with the desirable resonance frequency.

3.2.2 DC Power Supply

The supply of DC signals to the trap electrodes is much simpler to build. We need a multi-channel computer-controlled high-speed analog output and connect individual DC electrodes to it via a multi-pin feedthrough. The only caveat here is that we need to ensure the DC signals are free of undesirable AC noises. This can be done with simple low-pass filters (Figure 3.2). We definitely want to place one as close to the trap as possible inside the vacuum chamber; its cut-off frequency should be in the order of a few hundred kHz to filter out noises that would otherwise interfere with the secular motion of the trapped ions (see Table 2.2). The capacitor in this filter also has the additional job of explicitly grounding the DC electrodes at the RF frequency. As a result, its capacitance should be much larger than the trap capacitance, which is typically in the order of pF. The low-pass filter outside the vacuum chamber is optional and one can always choose its cut-off frequency and build it after experimenting without it.

⁹Mini-circuits is a good supplier of such simple circuits.

3.3 Creating Ultra-high Vacuum

Once wired-up to the power supplies, the trap will be sealed in the vacuum chamber, which will be pumped down to a UHV pressure. In theory, the lower the pressure in the vacuum chamber the more conducive it becomes for our experiment; in other words, a lower pressure means that there will be fewer unwanted particles around the trapped ions to interfere with their motion, transfer thermal energy to them or chemically react with them. In practice, we should be able to achieve a pressure that falls in the lower end of the UHV range, defined as pressures smaller than 10^{-7} Pa and greater than 10^{-10} Pa [11], without much difficulty. UHV range pressures should make it possible for us to trap ions for at least hours or even up to days.

The general procedure to achieve such a low pressure involves systematic cleaning of all surfaces inside the chamber, a few stages of pumping gases out of the vacuum chamber with a combination of pumps and a bake-out process, a method to remove mainly gas particles previously absorbed on the surface or in the bulk of materials. The instruments that will create, maintain and monitor the vacuum are connected to the chamber via a full nipple¹⁰ and a CF multiplexer¹¹ (Figure 3.1). The 2.75" port of the multiplexer will connect to an ion pump¹² while the four 1.33" ports will service an ion gauge, an angled valve, a needle valve, and a Titanium-sublimation (Ti-sub) pump respectively. The ion gauge measures the pressure in the chamber; the angled valve will isolate the vacuum system from the turbo pump that we will use for rough

¹⁰Kurt J. Lesker, FN-0275S

¹¹Kimball Physic, MCF275-FlgMplxr-C1r1A4

¹²Agilent, VacIon Plus 40-75

pumping while the needle valve may be needed in the future for introducing a gas into the chamber for co-trapping with ${}^9\text{Be}^+$.

The rest of the section will introduce the minimum theoretical basics required for designing a procedure for creating the UHV pressure we need. It will also include some discussion on material outgassing and choice of pumps. References [11], [12], [13], [14], Appendices G and H of [15], and Appendix B of [16] are highly informative on these matters; further perusal of them should prove to be helpful for finalizing the procedure for achieving UHV environment in our system.

3.3.1 Pumping of the Vacuum System

We do not need to know much about the theory of creating a vacuum to be able to engineer our system; in fact, we can mostly model ours after similar systems in [5], [7], and [16]. Nevertheless, to ensure that our design will indeed achieve the degree of vacuum we need, some order-of-magnitude calculations with basic understanding of the flow and sources of gas in the vacuum system are crucial¹³.

The pump-down from atmospheric pressure will start with rough pumping using a turbo pump during a few days of bake-out process. This process raises the temperature of the entire vacuum system, typically to a few hundred degrees Celsius or whatever the maximum temperature the “weakest link” in the system could endure is, so as to release volatile compounds such as water and hydrogen from the materials in the chamber. Once the pressure of the

¹³The discussion in this section is based primarily on Chapter 1 of [14].

system reaches the working pressure (typically 10^{-3} to 10^{-2} Pa) of the UHV pumps (the ion and Ti-sub pumps), we will isolate the turbo pump from the vacuum system and switch on the the UHV pumps. At this point, two competing factors, namely the rate at which gases enter the vacuum system and the pump speed in the chamber, determine the ultimate pressure. One of the main contributor of the former is surface outgassing, defined as the rate at which gas particles previously absorbed on the surfaces of materials escape into the chamber. We can minimize this rate substantially by rigorous surface cleaning and pre-baking of vacuum components. Gases can also enter the vacuum chamber through actual and virtual leaks, both of which should be minimized by the appropriate design of the system. On the other hand, pump speed is a measurement of the effective pumping ability of the UHV pumps in the chamber. Specifically, the ultimate pressure P_{ult} relates to the two quantities by

$$P_{ult} = \frac{Q_i}{S} \quad (3.1)$$

where Q_i is the rate of constant flow of gas into the vacuum chamber and S is the pump speed inside the chamber. Our procedure for creating the desirable degree of vacuum therefore involves minimizing Q_i and choosing the appropriate combination of pumps to achieve the matching S .

Since the major component of Q_i is surface outgassing, we can expect it to be a function of the total surface area of all components in the chamber itself. We will examine the other sources of Q_i in detail and estimate its magnitude in Section 3.3.2. On the other hand, the pump speed S in the vacuum chamber is a function of the designed pump speed S_0 of the two UHV pumps and the

conductance C of the components connecting them to the vacuum chamber:

$$S = \left(\frac{1}{S_0} + \frac{1}{C} \right)^{-1}. \quad (3.2)$$

Equation 3.2 shows that the effective pump speed inside the vacuum chamber S is always smaller than S_0 and we should maximize C in order to get the most out of the UHV pumps. In other words, ideally the pumps should be pumping gas directly out of the chamber. In practice, we are going to put some distance between the pumps and the chamber because putting them right against it at one of 2.75" CF ports would make it difficult to use the adjacent ports for optical access. Modelling the components linking the pumps and chamber as a short cylindrical tube, we can estimate C according to

$$C = \pi r^2 \left(\frac{k}{2\pi} \right)^{1/2} \left(\frac{T}{m} \right)^{1/2} \left(1 + \frac{3L}{8r} \right)^{-1}, \quad (3.3)$$

where L and r the length and radius of the short tube respectively, k the Boltzmann constant, T the temperature inside the vacuum system, and m the molecular or atomic mass of the species of gas been pumped out [14]. Considering both equations 3.1 and 3.2 as well as estimates of Q_i and C , we should be able to choose the appropriate combination of pumps to achieve the degree of vacuum we desire.

3.3.2 Sources of Gas in Vacuum

In this subsection, we will estimate Q_i by considering two major sources of gas particles inside the vacuum system, namely virtual leaks and outgassing

from the surface of materials. Although there are other sources of Q_i , we have identified the two as the most significant and also the ones with obvious remedies. [11] and [14] both offer excellent surveys of other potential problems and their solutions. Specifically, Chapter 22 of [11] and Chapter 8 of [14] deal with leak detection and should be a start to figuring out other possible problems that are not mentioned here.

In a vacuum system, we always want to avoid virtual leaks, which are sources of gas that are trapped in mechanical spaces, such as cracks and cavities, of in-vacuum devices. An example of a source of virtual leaks is the space inside a threaded hole that is not filled by the volume of the screw in it (Figure 3.4). Gas particles trapped in enclosed but not air-tight cavities are difficult to pump out during the bake-out and rough pumping stages but are nevertheless going to eventually escape into the vacuum due to the pressure difference between inside and outside the cavity. Hence virtual leaks increase pressure inside the vacuum chamber and also the time required to achieve a certain low pressure. Our ion trap, therefore, is engineered to prevent virtual leaks. There are no blind holes to create completely enclosed cavities; all threaded holes have either a pilot hole or are drilled through from the side (see Appendix A and pay special attention to the electrodes). If designs of other in-vacuum parts incorporate these virtual-leak precautions, contributions to Q_i by this type of leak after the bake-out and rough pumping stages should be negligible.

Surface outgassing is then the major player here. Its magnitude depends on the nature of materials inside the vacuum system and the total surface

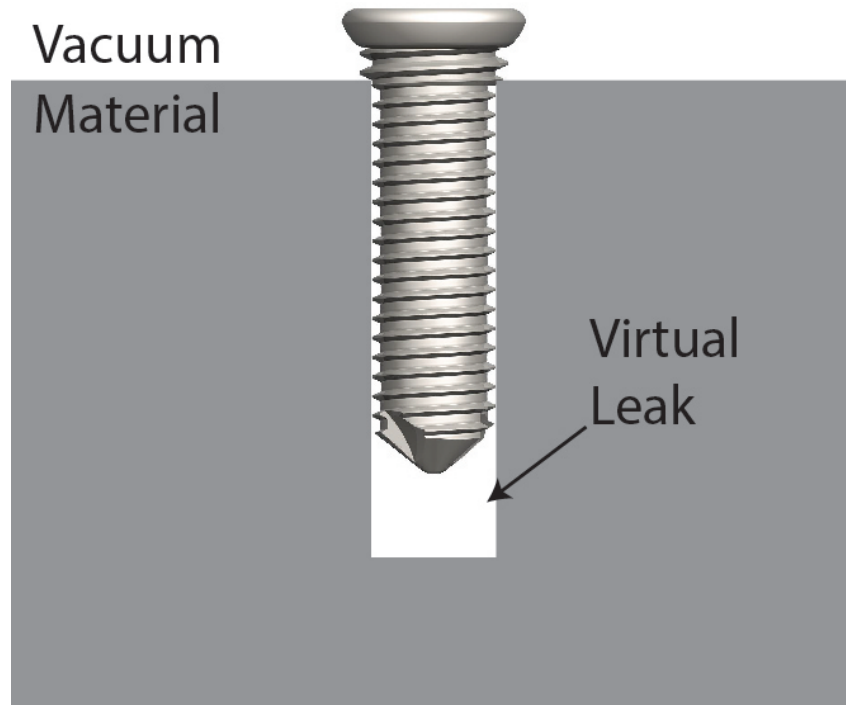


Figure 3.4: An example of virtual leak due to air trapped inside a cavity enclosed in a threaded hole.

area of these material. Certain materials used to make our trap, for instance OFHC copper for the electrodes, are chosen because they will have relatively low outgassing rates in vacuum. To estimate the order of magnitude of total outgassing, we can approximate the vacuum chamber as an enclosed cylinder and then calculate its inner surface area; most of the surfaces are made of stainless steel except for the six out of the eight 2.75" CF ports and the top 8.00" CF port, which are made of fused silica. The total surface area of stainless steel in the Kimball Physics spherical-octagon (MCF800-SphOct-G2C8) vacuum chamber is about 0.04 m^2 . Assuming that stainless steel is the only material that releases significant amount of gas in UHV and using the data from Appendix C of [11] for 316L stainless steel, we estimate Q_i to be about

2×10^{-11} W.¹⁴

Our estimate of the surface outgassing rate assumes a standard cleaning procedure. This number may potentially be further reduced by utilizing more rigorous surface cleaning techniques or potentially coating our electrodes with gold. Chapter 6 of [13] offers some general considerations on designing a cleaning procedure; Appendix H of [15] and Appendix B of [16] both contain cleaning procedures of UHV parts that have been used and tested by other research groups. It is difficult to tell at this point which methods of cleaning are absolutely necessary. On the other hand, coating the trap electrodes with gold, which seems to be favored by other groups¹⁵ that have built similar traps, may reduce the roughness of surfaces and thus the effective surface area. In theory, outgassing can be consequently reduced. So far not much has been done for designing the actual procedure; the next logical step should be examining standard practices, looking into the benefits of pre-baking in-vacuum parts as well as coating of electrodes with gold¹⁶.

3.3.3 Choice of UHV pumps

After estimating Q_i to be about 2×10^{-11} W, we are now in the position to specify the pump speed we need from our UHV pumps. Modelling compo-

¹⁴Notice that the dimension is given in W, which is Pa m³ s⁻¹; since pump speed S is given in m³ s⁻¹, equation 3.1 is correct dimension-wise.

¹⁵See [5]. Coating of electrodes with gold may be beneficial for reasons that are not the one stated here. Further investigation into the subject is needed to determine if it is worthwhile to do it.

¹⁶That being said, the author is skeptical about the value of putting too much time and effort into optimizing the cleaning procedure. Given that hours and manpower that is needed for working on other parts of the apparatus, it may be best that we follow someone else's procedure that has proven to work but may not be the optimal.

nents connecting the UHV pumps to the chamber as a single cylindrical tube of length 4.93" and radius 2.75" and using equation 3.3, we estimate their combined conductance to be approximately 41 L s^{-1} for nitrogen gas. Therefore, if we desire the ultimate pressure to be in the order of 10^{-9} Pa , it follows from equations 3.1 that we need the effective pump speed in the vacuum chamber to be about 20 L s^{-1} . According to equation 3.2, we need the combined pump speed (designed) of the two UHV pumps to be about 39 L s^{-1} .¹⁷ Noticeably, the effective pump speed inside the chamber can never exceed that of the conductance of the components connecting the chamber to the pumps; nor can it exceed the designed pump speeds of the UHV pumps.

We have chosen to use an ion pump and a Ti-sub pump as our UHV pumps because this combination have been the standard practice in creating UHV needed for ion trapping and storage. The ion pump works by ionizing gas particles inside the vacuum chamber and essentially trapping them; the Ti-sub pump, on the other hand, contains a filament of Titanium that is periodically heated and then deposited on a surface in a thin-film layer, which acts as the active surface that absorbs gases in vacuum. We are using two pumps to ensure that all kinds of gases that may normally be present in the vacuum chamber get pumped. The Ti-sub pump is most efficient at pumping oxygen and carbon monoxide; it will not, however, pump inert gases because the pumping process is essentially chemical. The ion pump will pump almost everything, including inert gases.

Given our calculations above, one of the Agilent, VacIon Plus 40-75 ion

¹⁷Pump speed is also a function of pressure and gas type. So the estimate here is only an average and truly an order-of-magnitude estimate.

pumps, combined with another commercially available Ti-sub pumps with pump speed in the same order of magnitude¹⁸, should be able to achieve a pressure as low as 10^{-9} Pa. The pump speed of the Ti-sub pump is usually given in terms of $\text{L}^{-1}\text{s}^{-1}\text{cm}^2$ for different types of gases; therefore the area that we eventually choose for depositing titanium inside the vacuum system will determine the pump speed. More research and enquiry into a commercially available Ti-sub pump should enable us to make a purchase of both UHV pumps soon.

In short, in order to create the UHV environment, we will have to create a comprehensive procedure starting from initial treatment of in-vacuum parts to the detection of leaks after the environment has been created. So far we have worked out the physical layout of the system and made some preliminary decision on the choice of UHV pumps. We still need to finalize a detailed procedure on pre-vacuum treatment of in-vacuum parts, including pre-baking in air [17] or vacuum [16] and surface cleaning. More research needs to be done on how exactly the bake-out process and the different stages of pumping will take place. Finally, to prepare for the worst, a systematic method of detecting leaks needs to be developed.

¹⁸The assumption here is that the two pumps will be pumping different gases, with the ion pump mainly taking care of inert gases that the Ti-sub cannot pump. Therefore, the pump speed for every species should be about the same order of magnitude in order to simultaneously lower the partial pressures of all gases present.

3.4 Imaging System

Finally, after being able to trap ions in UHV, we want to be able to look at them and also count how many of them we have trapped. The imaging system in its most basic form therefore involves an objective, which will be a series of lenses, able to resolve individual trapped ions up to a certain population size and project the magnified image of the ions into either a camera or a photomultiplier tube (PMT). In this section, we will discuss the specifications of the objective, which needs to be custom-made, and the camera, which we have already purchased, in the context of imaging ${}^9\text{Be}^+$.

There are a few factors at play in choosing the specifications for the objective. Firstly, the objective will “collect” spontaneously emitted photons (313 nm) as a population of excited trapped ions decays to the ground state; that means it needs to have a large enough numerical aperture to collect enough photons per second to trigger the camera or PMT. At the same time, it should be able to resolve individual ions trapped in the same potential well up to a certain population. Finally, it should magnify that dimension it has resolved so that it spans a certain minimum number of pixels of the camera.

We image trapped ions by pumping them up to an excited state using a laser (313 nm). At saturation, one single ion has a 50% chance of being in the excited state and the objective will collect only spontaneously emitted photons, which will travel with roughly equal probability in every angle. We can estimate the rate of spontaneous emission from the natural linewidth of the transition and our camera has a 25% efficiency for 313 nm and needs 10^5 photons per second to register a signal. Consequently, we need a mini-

numerical aperture of approximately 0.11 to collect enough photons for the camera to register this trapped ion. Since the numerical aperture N.A. = $\sin\left(\arctan\frac{d}{2L}\right)$, where L is the working distance and d is the diameter of the objective, it provides us with a ratio between d and L. For instance, if the objective has a working distance of about 50 mm¹⁹, it needs a minimum diameter of about 11 mm. To be on the “safe” side, it is always better to choose an objective with a higher numerical aperture, 0.5 for instance, provided it does not significantly increase the cost of making it.

On the other hand, we want to be able to resolve individual ions in the same trapping region. In order to determine the desired resolution, we have arbitrarily decided that the objective should be able to resolve a string of 14 trapped ${}^9\text{Be}^+$ ions. This translates into about a 5 μm separation between the two ions in the center²⁰, which means a resolution of 1 μm for the objective will be able to resolve the two ions as two clearly distinct particles (Figure 3.5). Subsequently, the objective should be able to magnify this resolution, say 1 μm , to at least a minimum number, say five, of pixels. For the camera we have purchased²¹ which has a single pixel size of 8 μm , that means we need

¹⁹This working distance means the objective will be outside the vacuum chamber, as shown in Figure 3.1. We have considered the possibility of placing it inside the chamber, which has its advantages and disadvantages. One of the reasons for doing so is that we can get the same numerical aperture with a smaller diameter for the objective by placing it closer to the trap, which generally means it will be cheaper. But in order to adjust the positions of the objective for focusing, some groups have installed it on an in-vacuum piezo-stage positioner [7], which is costly. In the end, we consider it a better alternative to place the objective outside the chamber right against the top 8" CF flange for the ease of focusing and also a significantly lower cost.

²⁰This calculation is done by assuming the ions are point charges inside a pseudo-potential well and each of them generates its own coulomb potential. The position of each ion is obtained by minimizing the total potential energy of the system. See [18] and [19].

²¹Andor iXon3-885 DU-885K-CS0-#VP

a magnification of 40.

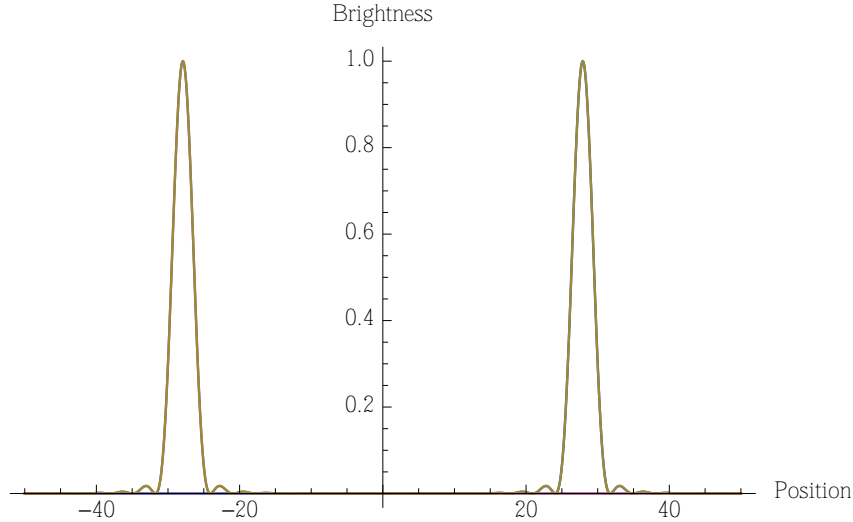


Figure 3.5: A “cross-section” of what two point sources, which are two trapped ions, look like through a circular aperture with N.A. = 0.5. The axes are not strictly calibrated to literally measure brightness or position but are proportional to those two parameters. The two ions are separated by about $5\ \mu\text{m}$. The objective has a resolution of $1\ \mu\text{m}$, a numerical aperture of 0.5, a working distance of 50 mm and thus a corresponding diameter of about 58 mm. It is clear that given the geometry of the aperture that is the objective, its $1\ \mu\text{m}$ resolution is powerful enough to completely resolve the two ions.

In short, here is our suggested specification for the assembly of lenses that is going to be the objective (Table 3.2). This assembly needs to be custom-made and the suggested specifications may not be the most cost effective, although it will certainly do its job.

These specifications can be handed over to an optics company for custom-making the assembly of lenses we need. We have been in touch with Sill Optics, a German company, for some preliminary design. Sill has offered us a design previously done for another customer and the working distance is 40 mm, 10 mm shorter than the 50 mm distance that we may have to place between the

Resolution	1 μm
Numerical aperture	0.5
Magnification	40
Working distance	50 mm
AR coating	a broad band that covers 280 - 400 nm

Table 3.2: Suggested specifications for the assembly of custom-made lenses that will act as the objective

objective and the trapped ions. This particular design is in production and costs \$5000. A completely new design will cost perhaps five times as much in engineering and production with Sill. It may be difficult but still possible to bring our objective to as close as 40 mm to the trap center while keeping it outside the vacuum chamber. We can also seek another optics company which may be able to meet the specifications in Table 3.2 with a lower cost.

Although we have already constructed a linear Paul trap and have done some preliminary designs for all three subsystems of the rest of the apparatus, namely the power supplies for the electrodes, the UHV system, and the imaging system, our journey towards performing high-precision spectroscopy on co-trapped ions is far from finished. Also, besides the Paul trap system described in Chapters 2 and 3, we need to construct the lasers and optics necessary for controlling, interrogating and imaging trapped ions, which is out of the scope of this thesis. Nevertheless, it is still useful and perhaps inspiring to keep our eyes on the prize and take a look at our final destination in the next chapter.

Chapter 4

Our Final Destination: Measuring the Time-variation of Electron-Proton Mass Ratio

The purpose of constructing the Linear Paul trap system is to house our experiment that will eventually measure the time-variation of electron-to-proton mass ratio (μ) by high precision frequency metrology. Such time dependence of μ arises naturally from theories of quantum gravity, which motivate our proposed laboratory work. Although there have been numerous efforts in quantifying $d\mu/dt$, we are confident that our proposed experiment may lead to a better assessment of the variation. The principal idea behind our experiment, namely quantum logic spectroscopy, may not only result in a new limit for the time-variation of μ but will also allow us to develop a novel method for performing spectroscopy with diatomic molecular ions.

4.1 Theoretical Motivations

In our ever-expanding Universe it actually makes sense to consider the possibility of spacetime dependence in the “constants” of nature over time during evolution of the Universe [20]. Paul Dirac proposed the large-number hypothesis (LNH), which asserts that all the large dimensionless numbers occurring in Nature, such as the age of the Universe, are connected with the present epoch, expressed in atomic units, and thus vary with time. The LNH requires variations of certain free parameters in our physical theories, such as the gravitational constant G [21]. The simplicity of the LNH and its large predictive power has led to continuous theoretical and experimental efforts in the search of time-variation of fundamental constants [22].

In unified theories of fundamental interactions, dimensionless constants such as the fine structure constant α , and μ are not necessarily constant [23]. For instance, generalized Kaluza-Klein (KK) models, which offer the attractive possibility of unifying gravity and other fundamental forces, enlarge spacetime into $4+N$ dimensions and predict that if the mean KK radius of the extra dimensions expands, contracts or oscillates, we would observe time-variations of “constants” in our conventional four dimensions [24]. Superstring theories, in addition, also offer a framework in which the values of fundamental constants can vary [23]. Consequently, experimentally examining the possibility of time-variation of parameters that we have assumed to be spacetime-independent can potentially lead to confirmation or rejection of unifying theories.

The dimensionless ratio μ is an especially important candidate for this particular investigation. Firstly, it is crucial that we observe the time-variation of

a dimensionless quantity. Even nominally dimensional quantities, for example length, are in fact ratios to arbitrary standards chosen to be units. Since our definition of units and the values of fundamental constants are entangled in such a way that any measurement of dimensional quantities is dependent on definitions of units, it only makes sense to consider the time-dependence of dimensionless quantities [23].

Secondly, time-variation in μ , if non-zero, has profound implications on our understanding of fundamental interactions. The electron, as an elementary particle, derives its mass directly from the Higgs mechanism via the electroweak interaction [25]. On the other hand, the bulk of the proton's mass comes from the quantum chromodynamics binding energy of the gluons, gauge bosons of the strong interaction, that hold the three quarks in the proton together [25]. Therefore, time-variation in μ will indicate a time dependence of the relative strength between the electroweak and strong interactions.

Theoretical speculations as well as the ramifications of such measurements have motivated searches for bounds of the time-variation in μ from both astronomical and laboratory data. These bounds have provided us with a standard of precision which we hope to improve by designing a novel experiment. The experimental methods of previous laboratory searches have also offered insights into the kinds of systematic effect that generally limit the precision of such measurements.

4.2 The Stability of μ

It is first pointed out by R. Thompson in 1975 that molecular absorption lines can provide a revenue for measuring the time-variation of μ [26]. According to Thompson's reasoning, the energy difference between two rotational levels scales as Mr^{-2} , where M is the reduced mass and r is the bond-length. In the case of molecular hydrogen, the electronic transitions scale as m_e while $M = m_p/2$; comparing purely rotational transitions with electronic transitions gives a measurement of μ .

Following Thompson's reasoning, the frequency ν of a vibration-rotational transition, in the Born-Oppenheimer approximation, scales as

$$\nu \propto (c_{elec} + c_{vib}/\sqrt{\mu} + c_{rot}/\mu), \quad (4.1)$$

where c_{elec} , c_{vib} and c_{rot} are respectively constants of proportionality intrinsic to the electronic, vibrational and rotational components of the transition in a diatomic molecule under observation. The relation in equation 4.1 is the very theoretical basis of previous research efforts aiming to put bounds on the size of the time-variation of μ . Both [23] and [27] offer more comprehensive reviews of recent results. One general approach is comparing the ratios of wavelengths of various electronic-vibration-rotational transitions in astrophysical spectra, obtain a measurement of μ and compare it with present day laboratory value. Another approach is comparing transition frequencies obtained through high-precision molecular spectroscopy. Right as this chapter was being drafted, a result with currently the highest precision from radio-astronomical observa-

tions of PKS1830-211 was published in [28]. Bagdonaite et al. deduced a constraint of $\delta\mu/\mu = (0.0 \pm 0.1) \times 10^{-7}$ at $z = 0.89$, corresponding to a look-time of 7 billion years. Another comparable result, which is referred to in the next section, published in 2011 sets the limit of $\Delta\mu/\mu$ at $< 3.6 \times 10^{-7}$ over 6.2 Gyr [29]. The best model-free result of $\frac{1}{\mu} \frac{\delta\mu}{\delta t}$ from laboratory spectroscopy data is $(-3.8 \pm 5.6) \times 10^{-14} \text{ yr}^{-1}$ [30].

4.2.1 Bounds from Astronomical Data

Redshifted absorption spectra of molecules from distant quasars provide an excellent source of data for calculating what the value of μ used to be when the light was emitted billions of years ago. Results from analyzing these molecular spectra, however, currently provide us with conflicting conclusions as to whether μ changes over time. For a comprehensive review of recent results, one can refer to the introduction of [29].

Re-analysis of H₂ spectral lines observed in Q 0347-383 and Q 0405-443 quasars by Reinhold et al [31], published in 2006, gives a weighted fractional change in μ of $\Delta\mu/\mu = (2.4 \pm 0.6) \times 10^{-5}$ over the past 12 billion years. Currently, this is the best result that predicts a non-zero time variation, particularly a decrease, in μ over cosmological time-scale at a 3.5σ confidence level.

When two molecular energy levels have different dependencies on μ , the spectral line wavelength representing a transition from one level to the other is sensitive to changes in μ . A coefficient K_i is a numerical evaluation of this relative sensitivity. Consequently, after compensating for cosmological

redshift, K_i relates the fractional change of μ to the ratio of the absorption line wavelength λ_i in the quasar absorption system to that in the present day rest-frame λ_i^0 via

$$\lambda_i/\lambda_i^0 = 1 + K_i\Delta\mu/\mu. \quad (4.2)$$

By including deviations from the Born-Oppenheimer approximation in their model, Reinhold et al. derived an improved calculation of K_i , which makes their analysis better than previous ones [31]. They also had a set of high-quality observation of H₂ spectrum as well as more accurate present-day H₂ spectroscopic measurements. With the set of improved K_i values and more accurate spectral measurements, $\Delta\mu/\mu$ was obtained by fitting the spectroscopy data and the K_i values to equation 4.2. The uncertainty in the final measurement of $\Delta\mu/\mu$ reflects both systematic errors in the measurements of transition frequencies, of H₂ in the present-day rest frame as well as that in the quasars, and how well the model describes the dependence of λ_i/λ_i^0 on the fractional change in μ .

Another strong limit, together with the presently strongest limit recently published in [28], obtained from astronomical data, however, contradicts the conclusion of the abovementioned analysis; an analysis of NH₃, Cs, and H₂CO spectral lines from the $z \sim 0.685$ absorber toward the quasar B0218+357 concludes that there is no statistically significant ($\geq 3\sigma$) evidence for changes in μ over the past 6.5 billion years and obtained a constraint of $\Delta\mu/\mu < 3.6 \times 10^{-7}$ at 3σ confidence level [29]. The model used in [29] is described in [32]. The analysis in [29] addresses directly most of the systematic effects in the next best result using NH₃ spectrum from the same quasar published

in [33]. But it is unable to quantify two possible sources of systematic errors: 1) the time variability in the background source morphology and 2) the possibility that nitrogen-bearing species such as NH_3 might arise at different velocities than the carbon-bearing species, to whose transition frequencies its own are compared.

By looking at the two contradicting conclusions, it becomes apparent that analyses of astronomical data are inherently difficult. The measurements of time-variation in μ are dependent on statistical models that determines which spectral lines are “good” for analysis. Moreover, there exist systematic effects extremely difficult to quantify; methods quantifying those that can be addressed are often model-dependent. Finally, if we want to obtain a rate at which the fractional change of μ varies with time, we have to again assume a model. Nevertheless, analyses of astronomical data have opened serious questions of the stability of μ . Precision measurements of molecular spectral frequencies in a controlled laboratory environment, on the other hand, can eliminate many systematic effects associated with astronomical data. It can also allow model-free calculation of the time-dependence of μ through comparison of spectral frequencies.

4.2.2 Bounds from Laboratory Spectroscopic Data

In the large majority of laboratory experiments measuring the temporal variations of fundamental constants, frequency measurements of two atomic clocks are compared; the fine structure constant α and the Rydberg constant R_y seem to be the most significant parameters studied [27]. Some examples of

model-free methods proposed for studying the time-dependence of μ involve measuring the vibrational energy intervals using ultracold Sr_2 trapped in an optical lattice [34], and studying certain narrow spectral lines in Cs_2 [35]. A recent model-free laboratory experiment comparing a molecular clock to an atomic clock measures $\frac{1}{\mu} \frac{\delta\mu}{\delta t}$ to be $(-3.8 \pm 5.6) \times 10^{-14} \text{ yr}^{-1}$ [30]. This result is consistent with zero and sets the standard of precision that we hope to surpass with our experiment.

The experiment, published in [30] by Shelkovnikov et al., measures the frequency of a molecular transition in SF_6 by interrogating a cold beam of SF_6 molecules with a CO_2 laser and compares it to an atomic transition in a Cs clock. The frequencies (ν) involved scale as $\nu(\text{SF}_6) = K_1 \sqrt{\mu} Ry$, and $\nu(\text{Cs}) = K_2 (\mu_{Cs}/\mu_B) \alpha^2 F(\alpha) Ry$, where K_1 and K_2 are constants indicating the relative sensitivity of the transition of changes in μ , μ_{Cs} is the magnetic dipole moment of the Cs nucleus, μ_B the Bohr magneton, and $F(\alpha)$ a dimensionless function counting for relativistic effects in Cs and is proportional to $\alpha^{0.83}$. The ratio of the two frequencies is clearly a function of μ , along with other “constants” α , μ_{Cs} and μ_B . By measuring the fractional change in this ratio over a period of time, one can calculate the fractional change in μ with respect to time by the equation below:

$$\frac{1}{\nu(\text{SF}_6)/\nu(\text{Cs})} \frac{\delta(\nu(\text{SF}_6)/\nu(\text{Cs}))}{\delta t} = -\frac{1}{2\mu} \frac{\delta\mu}{\delta t} - \frac{2.83}{\alpha} \frac{\delta\alpha}{\delta t} - \frac{1}{\mu_{Cs}/\mu_B} \frac{\delta(\mu_{Cs}/\mu_B)}{\delta t}. \quad (4.3)$$

To calculate the fractional change of μ over time, Shelkovnikov et al. used data for the fractional temporal variations of α and (μ_{Cs}/μ_B) obtained from atomic

clock experiments. There are two implications for using equation 4.3. Firstly, it means that the conclusion in [30] is model-free; it does not utilize any of the current models to derive the fractional temporal variations of α or (μ_{Cs}/μ_B) *ab initio* but uses the best empirical values instead. We prefer our future results to be model-free because that means we will have to make fewer assumptions about our system; a recent attempt using a Sr atomic clock to put a limit on the gravitational dependence of the fractional change in μ done Blatt et al., for instance, is less ideal since the group had used a model for calculating nuclear magnetic moments [36]. Secondly, in both cases of α and (μ_{Cs}/μ_B) the current limits are a factor of ten or more below the the calculated fractional change in μ [37]; that means the uncertainty in the calculation of the fractional temporal change of μ mainly comes from the statistical error associating with averaging the individual frequency measurements, and systematic effects inherent to the experimental method.

Reducing systematic effects is what a better experiment, such as the one we hope to perform, will have to achieve in order to improve precision and further push down the error bar. Sources of systematic errors that Shelkovnikov et al. have quantified in their study of the SF₆ transitions are mainly frequency shifts and noise in the lasers, changes in temperature and pressure of the molecular beam and blackbody radiation shifts (caused by changes in room temperature). Therefore, one way of improving the measurement of $\frac{1}{\mu} \frac{\delta\mu}{\delta t}$ is to design an experiment that avoids these sources of error.

Another approach to achieve an improved measurement is to ask the question that whether the transition interrogated in SF₆ is objectively the “best”

for performing high-precision metrology on molecules. In other words, the intrinsic properties of the transition measured may limit the precision that one can achieve in determining its frequencies. We are designing the experiment with the hope that it will bring about an increase in precision in the measurement of the time-variation of μ by addressing both of those aspects.

4.3 Search for the Most Suitable Diatomic Molecular Ion

The latter aspect of the two mentioned in the previous section, that of improving the precision of measurements of μ by choosing a “better” transition in a diatomic molecule, has been the subject of numerous research efforts. We consider primarily diatomic molecule because they have the simplest structure after the single-atom system. There are two criteria for determining if a particular transition in a certain diatomic molecule is good for spectroscopy. First, the transition should be sensitive to temporal changes in μ . In other words, we should use a transition in which the manifestation of a change in μ in terms of a frequency shift of the transition is maximized. Second, we should be able to in principle measure the transition frequency with maximum precision or minimum fractional error. This criterion also entails that the diatomic system should be simple enough that we can make corrections for all kinds of frequency shifts.

For a given physical system, there is a proportionality relation between $\Delta\mu/\mu$ and the corresponding fractional change in the transition frequency ν

associated with the change in μ ,

$$\frac{\Delta\mu}{\mu} = K \frac{\Delta\nu}{\nu}, \quad (4.4)$$

where K is the sensitivity coefficient and usually in the order of one. From equation 4.4, it is easy to see that $K = \frac{d\ln\mu}{d\ln\nu}$. Therefore, the uncertainty $\delta\mu$ as a fraction the measurement of μ can be expressed as a function of the uncertainty $\delta\nu$ in the measurement of ν :

$$\frac{\delta\mu}{\mu} = K \frac{\delta\nu}{\nu} = \frac{d\ln\mu}{d\ln\nu} \frac{\delta\nu}{\nu} = \left(\frac{d\nu}{d\ln\mu}\right)^{-1} \delta\nu. \quad (4.5)$$

In order to keep up with the notation here, one must remember that δ always indicates uncertainty and d derivative while Δ represents a change in a physical parameter. Equation 4.5¹ basically tells us that for a given set of experimental constrains that limit how small $\delta\nu$ is, we need to maximize $\frac{d\nu}{d\ln\mu}$ in order to obtain the minimum fractional uncertainty in the measurement of $\Delta\nu$. In other words, the highest possible precision can only be achieved if we choose to measure a transition where the maximum absolute frequency shift arises from a given fractional change in μ .

Studies of Cs₂ and Sr₂ in [35] and [34] respectively are examples of efforts looking for such transitions. In their study of Cs₂, DeMille et al. [35] approximate the vibrational energy levels E_v in order to find those that will render the maximum absolute frequency shift. They find the the energy sensitivity

¹The last step in the derivation of equation 4.5 assumes that the experimental limitations constrain $\delta\nu$ rather than the fractional uncertainty.

of E_v to be

$$\Delta_\mu E_v = \frac{v + 1/2}{2\rho(E_v)}, \quad (4.6)$$

where v is the quantum number for the vibrational energy levels and $\rho(E_v) = (\delta E_v / \delta v)^{-1} \approx (E_v - E_{v-1})^{-1}$ is the energy density of states at energy E_v . From equation 4.6 and the classical approximate of $\rho(E_v)$, DeMille et al. concludes that near its minimum where the typical potential is harmonic, $\Delta_\mu E_v$ gets an approximately v -fold enhancement for the v th vibrational level; in other words, near the ground state $\Delta\nu$ due to a given fractional change in μ increases with the quantum number v . For large values of v and E_v near the dissociation limit of the molecule, although the potential is not harmonic $\rho(E_v)$ also increases with increasing v . Hence, the value of $\Delta_\mu E_v$ decreases with increasing v for the highest energy levels. This implies that at some intermediate quantum number v , ΔE_μ and thus $\delta\nu$ and the fractional change in μ are maximized. In [34], an essentially similar theoretical argument is used to reach the same conclusion with Sr_2 . Determining this quantum number therefore addresses the first criterion mentioned earlier in this section.

On the other hand, since systematic effects and thus $\delta\nu$ in the measurement of ν are often proportional its magnitude, in order to partially address the second criterion of minimizing the fractional error of our measurement one can aim to maximize $\Delta\nu/\nu$; assuming that $\Delta\nu$ is already maximized, we can do so by minimizing ν . One way to achieve this goal without compromising the first criterion discussed above is to choose two close-lying molecular electronic potentials X and Y, with potential 0 and E_Y respectively [35]. In this case, an excited level highly sensitive to changes of μ in X with vibrational quantum

number $v_X \gg 1$ and energy E_{v_X} can be really close to a lower vibrational level that is less sensitive to μ in Y with energy $E_Y + E_{v_Y}$. Consequently, the frequency ν of this transition that one measures is small because the total energy difference between the two states is small; but the sensitivity of the transition to fractional changes in μ is still in a sense maximized.

Zelevinsky et al., on the other hand, choose find a transition that exclusively maximize sensitivity to changes in μ without trying to minimize $\delta\nu$. Their all-optical approach maximizes sensitivity through the cumulative effect of the entire molecular potential depth and is also expected to suppress certain systematic effects, although the microwave measurement proposed in [35] is going to have a smaller $\delta\nu$ [34]. In other words, Zelevinsky et al. choose to cover the first criterion really well in order to afford not doing so for the second criterion.

Both DeMille et al. and Zelevinsky et al. are looking for a transition in diatomic molecular systems that they consider as “simple” to address. Cs_2 , the subject of interest in [35], has two low-lying, overlapping potentials: the deep $X^1\Sigma_g^+$ ground state and the shallower $a^3\Sigma_u^+$. DeMille et al. conclude that the near degeneracy between the $v_a = 37$ and the $v_X = 138$ levels provides an excellent example of a system with all the favorable properties discussed above. Cs_2 is considered an ideal candidate for spectroscopy because all rovibrational levels in Cs_2 have long radiative lifetime ($\gg 1s$). The long lifetime makes it possible to yield spectral lines with narrow width (energy-time-uncertainty principle) and since the statistical uncertainty for measuring ν is directly proportional to this linewidth, Cs_2 inherently permits a more precise measurement

than molecules with states of short lifetime. Furthermore, the technology for reliably preparing ultracold Cs_2 in the $a^3\Sigma_u^+$ state is readily available.

Zelevinsky et al. choose to look at transitions in alkaline-earth-metal-type molecules, Sr_2 in particular, also due to the simplicity of those systems. The lack of electronic nuclear spin in the electronic ground state $X^1\Sigma_g^+$ of these molecules means that there is only one ground state rather than a hyperfine manifold. This allows reliable theoretical modeling and prediction of vibrational levels as well as better understanding and quantification of systematic frequency shifts. Furthermore, the zero angular momentum guarantees an absence of magnetic structure in the electronic ground state, simplifying the preparation of the initial states and reducing systematic effects. Finally, the existence of spin-triplet metastable states that have large Franck-Condon factors with the ground state guarantees narrow width of the spectral lines (and thus naturally reduced statistical uncertainty for frequency measurements) and ensures that very low laser intensities are needed to interrogate the molecules. Zelevinsky et al. conclude that certain transitions in Sr_2 between vibrational levels in the electronic ground state $X^1\Sigma_g^+$ and those in the metastable state 0_u^+ are highly sensitive to the fractional change in μ . They propose a scheme that compares the frequency of one of these transitions to that of the least sensitive one to the fractional change in μ .² The difference of the two transitions,

²In the experiment proposed by DeMille et al. in [35], the frequency transition chosen in Cs_2 for spectroscopy is compared to a Cs clock. That means it will eventually be given in Hz as the Cs clock defines the unit for time. However, given that the precision of frequencies reported in Hz is ultimately limited by the precision of the Cs clock, one would imagine that a scheme that promises a higher precision has to move away from reporting frequencies in Hz but instead report it as a ratio to another transition frequency in the same atom or molecule with which one is trying to perform precision metrology. The assumption behind this statement is that by measuring the frequency of a transition in another species, one has

normalized by their sum, doubles the sensitivity of the frequency measurements to the fractional change in μ while eliminating any drift in a frequency reference used to stabilize the frequency comb used in the proposed experiment (see [34] for details).

The moral of these two proposed experiments is that the transition in which we look for the time variation of μ sets the upper bound for the precision we could achieve, independent of the method of spectroscopy. On one hand, we need to choose a transition where its frequency experiences a maximum shift for a given fractional change in μ ; in order to find that transition we need a model (or models) for the vibrational energy levels in the diatomic molecule we are considering. On the other hand, this transition should be narrow, and the lifetime of the metastable state involved needs to be long enough so that the natural linewidth of the frequency is minimized while it should also be “simple” enough so that we can either quantify or minimize systematic shifts in its frequency. Choosing a molecule and a transition that have all the favorable properties above is essentially going to increase the precision of measurements relative to previous experiments via the second of the two approaches discussed in Section 4.2.2.

Noticeably, both [35] and [34] have pointed out the ease of cooling as an important consideration when choosing the diatomic molecule used in their respective experiments; essentially, the species chosen must have a transition available for laser-cooling so as to eliminate velocity-related systematic fre-

effectively built a new clock. It is likely that the transitions in this new clock are measured more precisely than those in the CS clock. Therefore, one should presumably be better off using another transition frequency in the new clock as the basis of comparison.

quency shifts. The next section will address the first of the two approaches mentioned in Section 4.2.2 for improving the precision of measurements of μ and its temporal changes by proposing a different method of spectroscopy. Since the new method involves sympathetic cooling of a diatomic molecular ion by an atomic ion instead of direct laser cooling, diatomic molecules that cannot be cooled directly and thus are not considered in [35] and [34] are now available to us for spectroscopy

As part of our preliminary effort to find the ideal molecule and transition, we have examined the molecular ion of oxygen $^{16}\text{O}_2^+$ as a possible candidate. Similar to Sr_2 , $^{16}\text{O}_2^+$ has no nuclear spin in its electronic ground state and therefore no hyperfine structure in the ground state. Moreover, $^{16}\text{O}_2^+$ has a deeply bound (dissociation energy is 6.663 eV [38]) ground state $X^2\Pi_g$ with 56 vibrational states; the one with $v_X = 21$ has a near degeneracy with the lowest vibrational state of the first excited state $a^4\Pi_u$. Using a generic Morse potential for modelling these vibrational states as in [34] and [35], we estimate the sensitivity of the $v_x = 21$ vibrational level in the ground state to the change in $\ln \mu$ to be $\frac{d\nu}{d\ln \mu} \approx 381 \text{ THz}$. This sensitivity is a little more than 50 times better than that estimated in [34], which is about 7.5 THz. In other words, by choosing a “better” transition alone we can expect at least an order-of-magnitude increase in the precision of our measurements of $\Delta\mu$. Further reducing systematic effects in the method of spectroscopy will only enhance our precision by lowering $\delta\nu$ as in equation 4.5.

4.4 Quantum Logic Spectroscopy

As mentioned in the previous section, the experiment we propose involves sympathetic cooling a molecular ion by an atomic ion, both of which are trapped in the same potential well in the linear Paul trap described in Chapter 3. As the motional modes of individual ions are coupled by Coulomb interaction, we can use the atomic ion to cool the molecular ion's rotational and vibrational degrees of freedom, efficiently prepare initial states and detect final states of the molecular ion. The method, known as quantum logic spectroscopy, deploys recently developed quantum information processing techniques and removes the requirements for efficient cooling, state preparation, and state detection from the species upon which the spectroscopy is performed [39].

4.4.1 How it works

Quantum logic spectroscopy has been demonstrated experimentally in [39] with an $^{27}\text{Al}^+$ sympathetically cooled to its motional (translational, vibrational and rotational) ground state by a $^9\text{Be}^+$. Although no such spectroscopy has been performed on molecular ion, [40], [8], and [41] have reported sympathetic cooling of the motional degrees of freedom of neutral and charged molecules. This section will describe the basic idea of quantum logic spectroscopy, the method that we hope to use to perform spectroscopy with a diatomic molecule, possibly $^{16}\text{O}_2^+$.

To describe the principle of quantum logic spectroscopy as in [39], we consider an atomic ion and a molecular ion, which we will designate as the logic

ion and the spectroscopy ion respectively, trapped in the same potential well of our linear Paul trap. We are interested in the normal modes resulted from the Coulomb interaction of the two ions. The internal states of the ions are represented by two eigenstates $|\uparrow\rangle_{L,S}$ and $|\downarrow\rangle_{L,S}$ ³ and each internal state accommodates motional states $|n\rangle_m$, where n represents quanta of motion. To start, we assume that all normal modes have been cooled to their ground states (Figure 4.1A) by laser-cooling of the logic ion, which sympathetically cools the spectroscopy ion. The initial state of the two ions can therefore be described by the wave function $\Psi_0 = |\downarrow\rangle_S |\downarrow\rangle_L |0\rangle_m$.

We will excite the spectroscopy ion with a laser tuned near resonance to the transition with which we have chosen to perform spectroscopy (Figure 4.1B). Consequently, the wave function becomes

$$\Psi_0 \rightarrow \Psi_1 = (\alpha |\downarrow\rangle_S + \beta |\uparrow\rangle_S) |\downarrow\rangle_L |0\rangle_m = (\alpha |0\rangle_m |\downarrow\rangle_S + \beta |0\rangle_m |\uparrow\rangle_S) |\downarrow\rangle_L, \quad (4.7)$$

where $|\alpha|^2 + |\beta|^2 = 1$.

Next, we apply a red sideband (RSB) π pulse to the spectroscopy ion (Figure 4.1C) so that

$$\Psi_1 \rightarrow \Psi_2 = (\alpha |\downarrow\rangle_S |0\rangle_m + \beta |\downarrow\rangle_S |1\rangle_m) |\downarrow\rangle_L = |\downarrow\rangle_S |\downarrow\rangle_L (\alpha |0\rangle_m + \beta |1\rangle_m), \quad (4.8)$$

thereby mapping the probability density of the spectroscopy ion being in each of its internal states after step B to its motional states. The key here is that

³The indices L and S denote the logic and spectroscopy ions respectively. The spin-up and spin-down symbols do not indicate the internal state to be necessarily a spin-1/2 system. In fact it is generally not.

the $|\downarrow\rangle_S |0\rangle_m$ portion of Ψ_1 is unaffected by the RSB π pulse since the state $|\uparrow\rangle_S |-1\rangle_m$ does not exist.

We then apply a different RSB π pulse to the logic ion so that

$$\Psi_1 \rightarrow \Psi_{final} = |\downarrow\rangle_S (\alpha |\downarrow\rangle_L + \beta |\uparrow\rangle_L) |0\rangle_m, \quad (4.9)$$

thereby completing the mapping of the spectroscopy ion's state after step B to the final state of the logic ion. Assuming that we can effectively detect $|\downarrow\rangle_L |0\rangle_m$, by repeating this experiment many times, we can determine the probabilities $|\alpha|^2$ and $|\beta|^2$ as a function of the frequency of the spectroscopy laser frequency used in step B. The frequency that corresponds to a minimum $|\alpha|^2$ or a maximum $|\beta|^2$ is therefore a measurement of the transition $|\downarrow\rangle_S |0\rangle_m \rightarrow |\uparrow\rangle_S |0\rangle_m$.

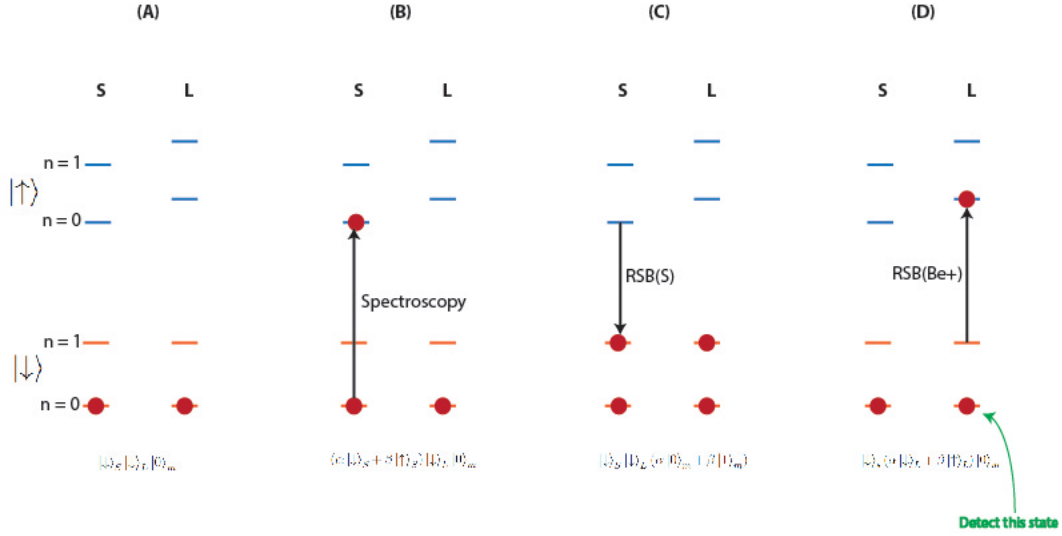


Figure 4.1: Quantum logic spectroscopy. (A) We start in $|\downarrow\rangle_S |\downarrow\rangle_L |0\rangle_m$, assuming all normal modes have been cooled to their ground states. (B) We will excite the spectroscopy ion with a laser tuned near resonance to the transition with which we have chosen to perform spectroscopy. (C) Next, we apply a red sideband (RSB) π pulse to the spectroscopy ion. (D) Finally, we apply a different RSB π pulse to the logic ion and detect the $|\downarrow\rangle_S |0\rangle_m$ state.

We plan to implement this technique, which has been realized with atomic ions in [39], with a ${}^9\text{Be}^+$ as the logic ion and a diatomic molecular ion as the spectroscopy ion. The feasibility of this technique with molecular ions then depends critically on if we can efficiently and reliably prepare the initial state in which ions need to be in at the start of this procedure.

4.4.2 Initial State Preparation

When we sympathetically cool the molecular ion with the atomic ion, typically excited electronic and vibrational states of the molecular ion will decay to their ground states within nanoseconds and milliseconds, and the rotational state distribution will follow a thermal distribution corresponding to the blackbody

temperature of the trap [42]. To prepare the initial state for spectroscopy with the molecular ion is therefore essentially manipulating its rotational state reliably and efficiently, and ideally without altering its electronic or vibrational state. The only other degree of freedom left here is the hyperfine structure of the molecule. Here we assume that it does not exist in the ground state, which will be true if we choose our spectroscopy ion wisely.

Schemes for rotational cooling of molecular ions, where the mass of the molecular ion is not too much larger than that of the atomic ion, have been proposed in [39] and [42]. The basic idea is to first apply a transfer pulse to the spectroscopy ion so as to drive a Raman transition (more on how to accomplish Raman transitions later) from the J th rotational state to, say, the $(J - 1)$ st rotational state, adding one quantum of motion in the process (Figure 4.2A). If in the case of linear and spherical-top molecules, $J \rightarrow J \pm 1$ transitions are forbidden, we will then drive the $J \rightarrow J - 2$ in those cases. The transition will only work in one direction because the other way, $|J - 1, n = 0\rangle \rightarrow |J, n = -1\rangle$ or $|J - 2, n = 0\rangle \rightarrow |J, n = -1\rangle$ is forbidden. We can then remove the one quantum of motion by ground state cooling to the atomic (logic) ion (Figure 4.2B), driving it to its excited state while removing a quantum of motion via another Raman transition. Eventually, we can detect the final state of the molecular ion by determining if the atomic ion has been excited (Figure 4.2C). If the molecular ion has been successfully transferred the $(J - 1)$ st or $(J - 2)$ nd rotational state, the atomic ion can be reset to the ground state by optical pumping without disturbing the rovibrational or electronic state of the molecular ion. In this way, rotational cooling of the molecular ion has been

achieved and the system is ready for further manipulation or spectroscopy as described in Section 4.4.1.

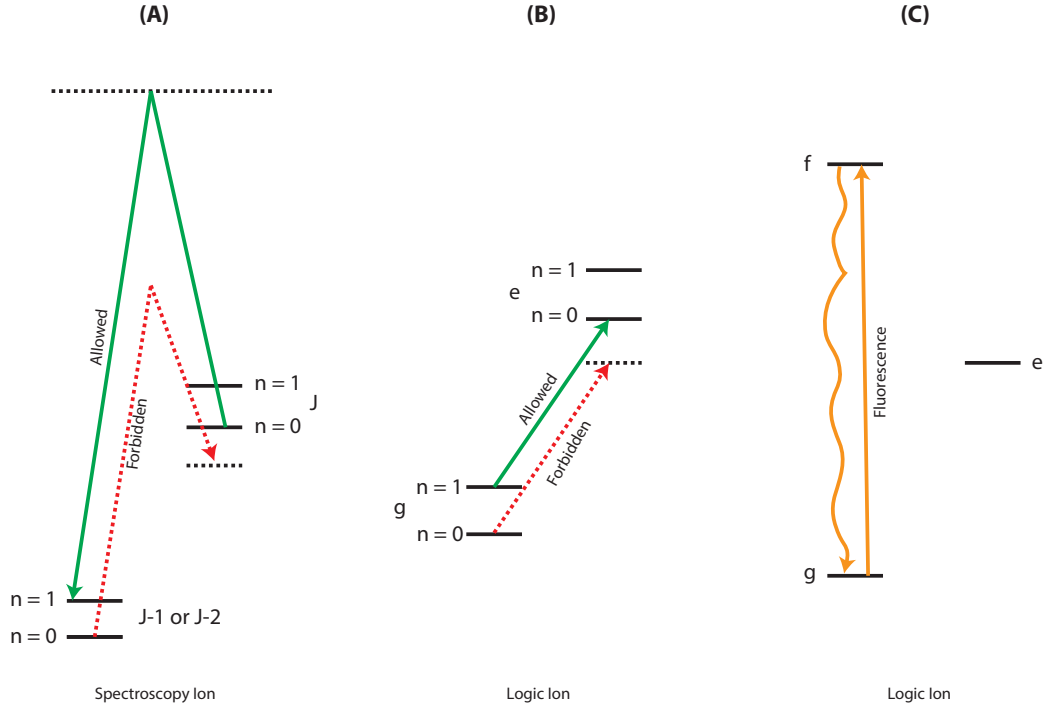


Figure 4.2: Rotational cooling of the spectroscopy ion (energy levels not to scale). (A) The spectroscopy ion undergoes a Raman transition from the J th rotational state to the $J - 1$ st or $J - 2$ nd state, gaining a quantum of motion. (B) Excitation of the logic ion from the ground state g to the excited state g . Since the motional states of the two ions are coupled, the spectroscopy ion will be in the $|J - 1, n = 0\rangle$ or $|J - 2, n = 0\rangle$ state as desired. (C) We can effectively detect the final state of the spectroscopy ion by detecting the electronic state of the logic ion. This is done by laser-induced fluorescence on a cycling transition connecting g and a fast-decaying state f . If there is no fluorescence, the logic ion is in the excited state e . It can then be restored to g by optical pumping.

The Raman transitions in the procedure described above are driven by two lasers, both detuned from resonance with an excited electronic state, and their relative detuning is equal to the transition frequency. If the transition frequency is small enough (in the order of MHz), the two lasers can be produced by splitting a continuous-wave laser and frequency-shifted with an acousto- or electro-optic modulator to create the frequency difference. If the transition frequency is in the order of many GHz or larger, we can drive it with a frequency-comb laser of equally spaced frequencies. In general, a large Raman transition of the molecular ion driven by a frequency-comb laser requires that the resonance condition

$$N\omega_m + \Delta\omega_0 = \Omega_{J,J\pm 1,2} + n\omega_{\pm} \quad (4.10)$$

is fulfilled. In equation 4.10, N and n are integers, ω_m the comb mode spacing, $\Delta\omega_0$ the frequency shift added by the modulator, $\Omega_{J,J\pm 1,2}$ the energy difference between two rotational states, and $n\omega_{\pm}$ is n quanta of motion [42]⁴. For instance, the resonance frequency for the $J \rightarrow J - 2$ transition ($\Delta J = \pm 1$ is forbidden) in the $^{16}\text{O}_2^+ X^2\Pi_{1/2g}$ ground state is 302.2 GHz; in order to drive this transition, we can use a comb that has 1 GHz mode spacing and an additional shift of 200 MHz from a modulator. In other words, $N = 302$ in this case.

As for the integer n in equation 4.10, transitions with $n = 0$ will have the largest transition rate, while the n th “sideband” will be suppressed by the n th

⁴ ω_+ and ω_- are frequencies of motional modes of the molecular and atomic ions, coupled by Coulomb interaction.

power of the Lamb-Dicke parameter. In our procedure, we will be driving the first sideband, which is the motion-altering state with the highest transition rate and changes the motional state by one quantum.

Furthermore, integrating the frequency-comb laser into quantum logic spectroscopy will enable rapid precise measurements of the rotational structure of many molecules. This in itself is an important experimental goal, with increases in precision of up to several orders of magnitude. We can in fact begin our research by probing the ground state rotation structure of $^{16}\text{O}_2^+$ so as to determine its sensitivity to the fractional change in μ .

To conclude, this chapter has provided some insights into the theoretical motivation of chasing our long-term research goal – measuring the time-variation in μ . A survey of previous research efforts has also provided us with some idea of the level of precision our experiment should strike for. Finally, we have also outlined a plausible experimental method that will enable us to perform high-precision frequency metrology that will eventually lead to better measurements of the time-variation of μ .

Chapter 5

Not A Conclusion

Since this thesis is not an end but rather a beginning of our ambition to measure the time-variation of μ , this final chapter is not meant to conclude. Instead, it takes a look at where we are currently and makes “to-do” lists that will take us further. We have done something for every part of the linear Paul trap system. We have also thought about our experimental method and how as well as why it will allow us to observe the time-variation of μ , potentially better than many other methods out there. In order to keep moving forward from what is already known and done towards our final destination, it is then useful to re-examine every aspect of our adventure addressed in this thesis and ask questions and consider what to do next.

In terms of apparatus building, we have constructed the assembly of electrodes for the trap based on the requirements of our proposed experiment (Chapter 2). Although we have a good understanding of how the linear Paul trap works and are confident that our electrodes will be able to confine a ${}^9\text{Be}^+$

ion and a diatomic ion, certain properties of the trap, such as the actual electric potential it produces, are unknown to us because we do not have a mathematical model for quantifying them. One interesting and potentially useful thing to do is to numerically simulate the electric potential generated by the trap electrodes with a electric field modeling software. The computer-generated model will allow us to calculate the trap frequencies of the trapped ions and these calculated frequencies will be closer to reality than those in Chapter 2. Knowing the trap frequencies more accurately will help us in the designing of other apparatus, such as the low-pass filters for the DC power supply, and may save us time later.

We also have a general idea of how the entire Paul trap system, including the power supplies for the electrodes, the UHV instruments and the imaging system, will come together (Chapter 3). In terms of power supplies, the helical resonator we need for generating the RF signal is ready to move on from the design phase to the construction and testing phase. To do so, we need to measure the trap capacitance and resistance, which are inputs in finalizing the geometric parameters in the helical resonator. The minimum steps we need to take are to install the trap in the vacuum chamber and make the electrical connections to the RF power feedthrough without creating the UHV just yet. So in order to construct the RF power supply, we need to develop a surface cleaning procedure to prepare all the in-vacuum surfaces for UHV environment before installing the trap for measuring its capacitance and resistance.

Finally, we have thought about our experimental method and how as well as why it will allow us to observe the time-variation of μ , potentially bet-

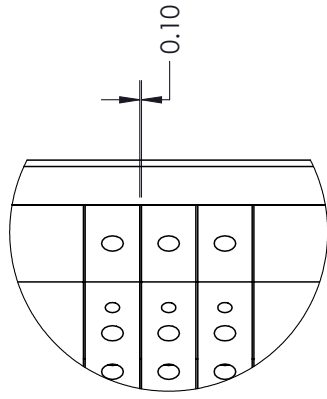
ter than many other methods (Chapter 4). The next important decision we have to make is perhaps the choice of the diatomic molecular ion to be used for spectroscopy. We can start by taking a closer look at the rovibrational transitions in our potential candidate $^{16}\text{O}_2^+$ and evaluate their “usefulness” for spectroscopy according to the criteria discussed in Section 4.3.

To sum up, there are a number of projects we can undertake simultaneously in the next few months to come. One of them is to develop the procedure for surface cleaning and creating the UHV environment. That also involves placing orders for commercially available parts because some of them may have a lead time as long as a number of weeks. Once we go ahead and install the trap in the vacuum chamber (creating the UHV is at the moment optional), we can then obtain the trap capacitance and resistance we need to finalize our design of the helical resonator. Meanwhile, we can continue to convince ourselves that $^{16}\text{O}_2^+$ or another diatomic molecular ion is exactly the one we want for quantum logic spectroscopy. Independent of the two projects mentioned above, some time and manpower should also be dedicated to searching for an affordable supplier to custom-make the objective. Finally, if time and resources allow, it may be worthwhile to numerically model the electric potential produced by the trap electrodes and thus produce more accurate estimates of secular frequencies.

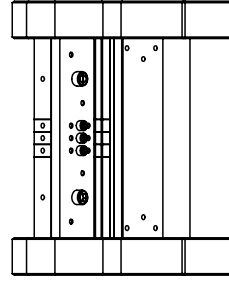
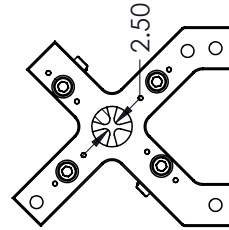
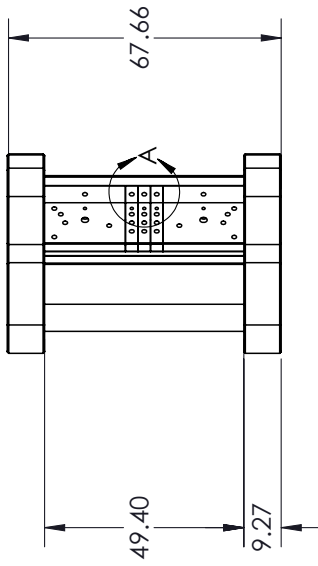
Appendix A

Machined Linear Paul Trap

Drawings



DETAIL A
SCALE 3 : 1



UNLESS OTHERWISE SPECIFIED:
DIMENSIONS ARE IN MM
TOLERANCES:
ANGULAR: MACH $\pm .5^\circ$ BEND $\pm .5^\circ$
TWO PLACE DECIMAL $\pm .025$ MM
THREE PLACE DECIMAL $\pm .013$ MM

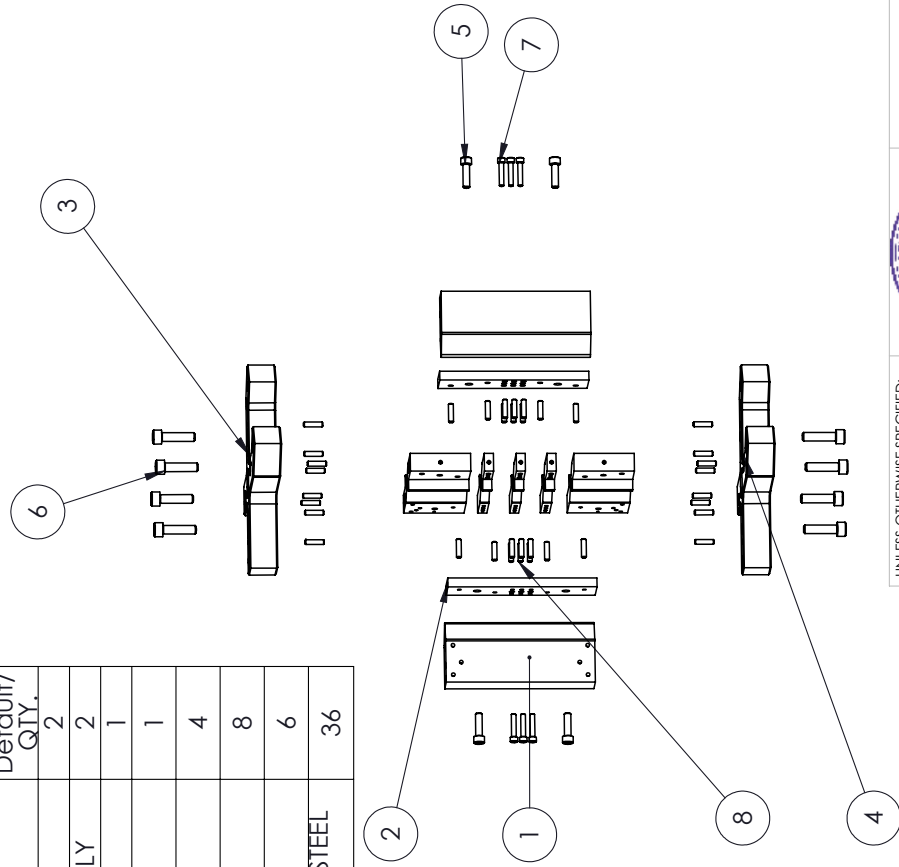


PHYSICS
DEPARTMENT

TITLE
RF TRAP

DO NOT SCALE DRAWING	NAME JMK	DATE 10/26/12	SIZE A	DWG. NO.	REV
	DRAWN	CHECKED			
	APPR				
			SCALE: 1:2	WEIGHT:	SHEET 1 OF 11

ITEM NO.	DESCRIPTION	Default/ QTY.
1	ELECTRODE	2
2	ELECTRODE ASSEMBLY	2
3	MACOR END	1
4	MACOR END	1
5	2-56 X 5/16" SHCS	4
6	4-40 X 7/16" SHCS	8
7	0-80 X 5/16' SHCS	6
8	1/16" X 1/4' STAINLESS STEEL DOWEL	36



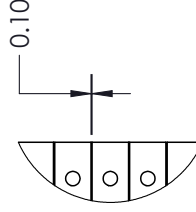
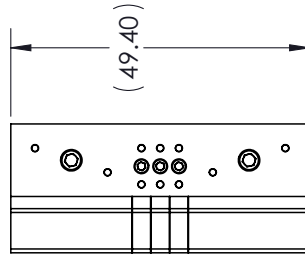
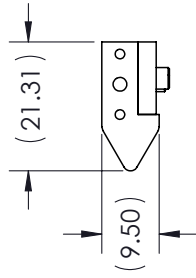
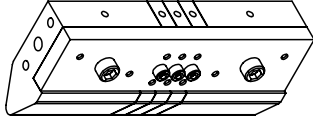
83



PHYSICS
DEPARTMENT

TITLE
RF TRAP

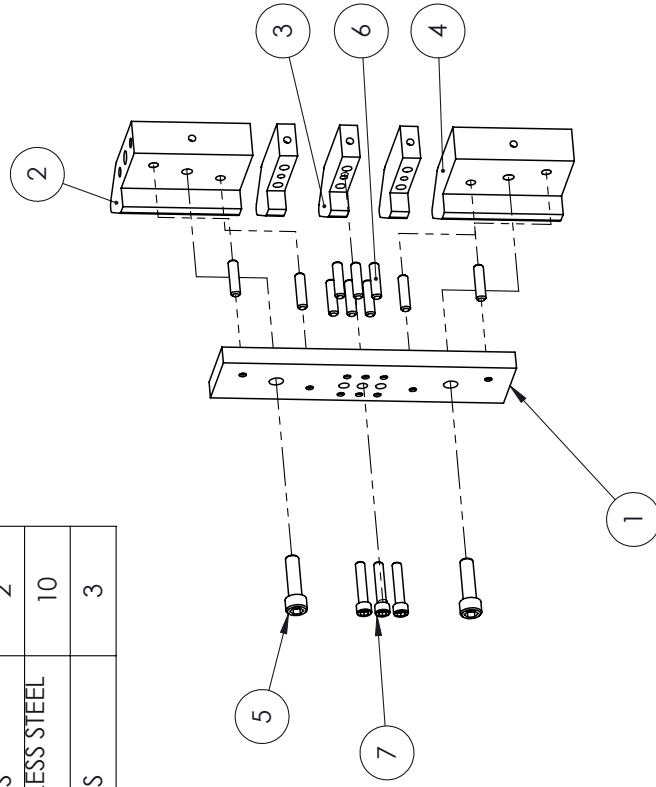
UNLESS OTHERWISE SPECIFIED: DIMENSIONS ARE IN MM TOLERANCES: ANGULAR: MACH $\pm .5^\circ$ BEND $\pm .5^\circ$ TWO PLACE DECIMAL $\pm .025$ MM THREE PLACE DECIMAL $\pm .013$ MM	NAME JMK	DATE 10/26/12	SIZE A	DWG. NO.	REV
INTERPRET GEOMETRIC TOLERANCING PER: MATERIAL FINISH	DRAWN	CHECKED	SCALE: 1:5	WEIGHT:	SHEET 2 OF 11
DO NOT SCALE DRAWING	APPR				



DETAIL B
SCALE 2:1

<p>UNLESS OTHERWISE SPECIFIED: UNLESS OTHERWISE NOTED DIMENSIONS ARE IN MM TOLERANCES: ANGULAR: MACH $\pm .5^\circ$ BEND $\pm .5^\circ$ TWO PLACE DECIMAL $\pm .025$MM THREE PLACE DECIMAL $\pm .013$MM</p>				<p>PHYSICS DEPARTMENT</p>	
<p>INTERPRET GEOMETRIC TOLERANCING PER:</p>		<p>TITLE ELECTRODE ASSEMBLY</p>		<p>DATE 10/26/12</p>	
<p>MATERIAL</p>		<p>NAME JMK</p>		<p>SIZE A</p>	
<p>FINISH</p>		<p>DRAWN JMK</p>		<p>DWG. NO. REV</p>	
<p>DO NOT SCALE DRAWING</p>		<p>CHECKED APPR</p>		<p>SCALE: 1:1 WEIGHT: SHEET 3 OF 11</p>	

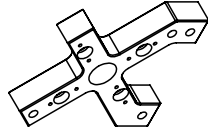
ITEM NO.	DESCRIPTION	QTY.
1	MACOR BASE	1
2	ELECTRODE W TOP	1
3	ELECTRODE N	3
4	ELECTRODE W	1
5	2-56 X 5/16" SHCS	2
6	1/16" X 1/4" LONG STAINLESS STEEL DOWEL	10
7	0-80 X 5/16" SHCS	3



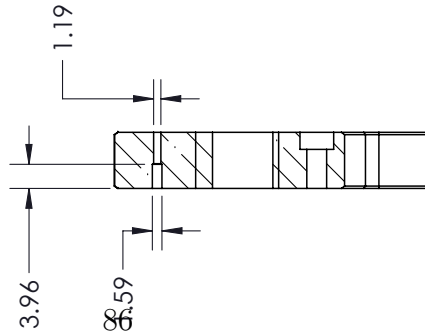
85

<p>UNLESS OTHERWISE SPECIFIED: DIMENSIONS ARE IN MM TOLERANCES: ANGULAR: MACH $\pm .5^\circ$ BEND $\pm .5^\circ$ TWO PLACE DECIMAL $\pm .025$MM THREE PLACE DECIMAL $\pm .013$MM</p>		<p>PHYSICS DEPARTMENT</p>	
<p>INTERPRET GEOMETRIC TOLERANCING PER:</p>		<p>TITLE ELECTRODE ASSEMBLY EXPLODED VIEW</p>	
<p>MATERIAL</p>		<p>SIZE A</p>	<p>DWG. NO.</p>
<p>FINISH</p>		<p>NAME JMK</p>	<p>REV</p>
<p>DO NOT SCALE DRAWING</p>		<p>DATE 10/26/12</p>	<p>SCALE: 1:2 WEIGHT:</p>
<p>3</p>		<p>DRAWN</p>	<p>SHEET 4 OF 11</p>
<p>4</p>		<p>CHECKED</p>	<p>1</p>
<p>5</p>		<p>APPR</p>	<p>2</p>

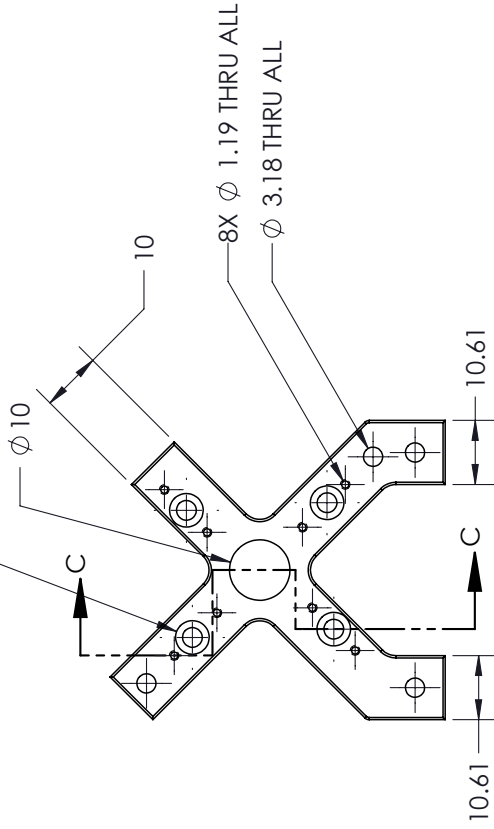
NOTES:
1. QUANTITY 2 REQUIRED



ϕ 3.26 THRU ALL
 ϕ 5.56 ∇ 2.84



SECTION C-C



9.27

UNLESS OTHERWISE SPECIFIED:

DIMENSIONS ARE IN MM
TOLERANCES:
ANGULAR: MACH $\pm .5^\circ$ BEND $\pm .5^\circ$
TWO PLACE DECIMAL $\pm .025$ MM
THREE PLACE DECIMAL $\pm .013$ MM

INTERPRET GEOMETRIC
TOLERANCING PER:

MATERIAL
MACOR
FINISH

DO NOT SCALE DRAWING



NAME	DATE
JMK	10/26/12
DRAWN	CHECKED
APPR	

PHYSICS
DEPARTMENT

TITLE
MACOR END

SIZE	DWG. NO.	REV
A		
SCALE: 1:1	WEIGHT:	SHEET 5 OF 11

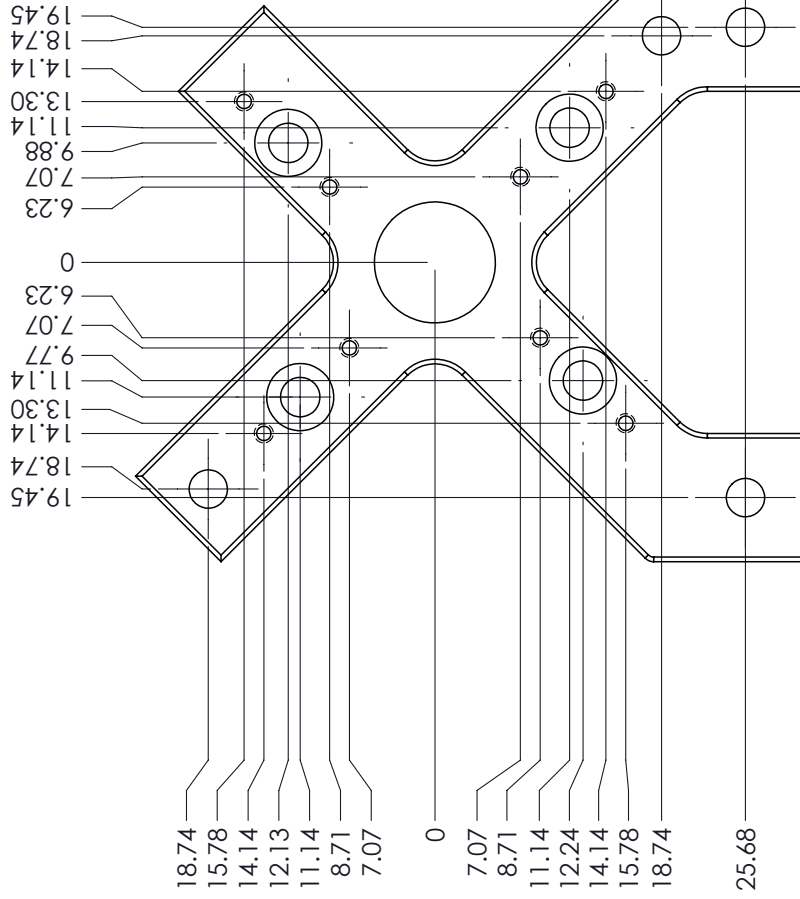
5

4

3

2

1



87



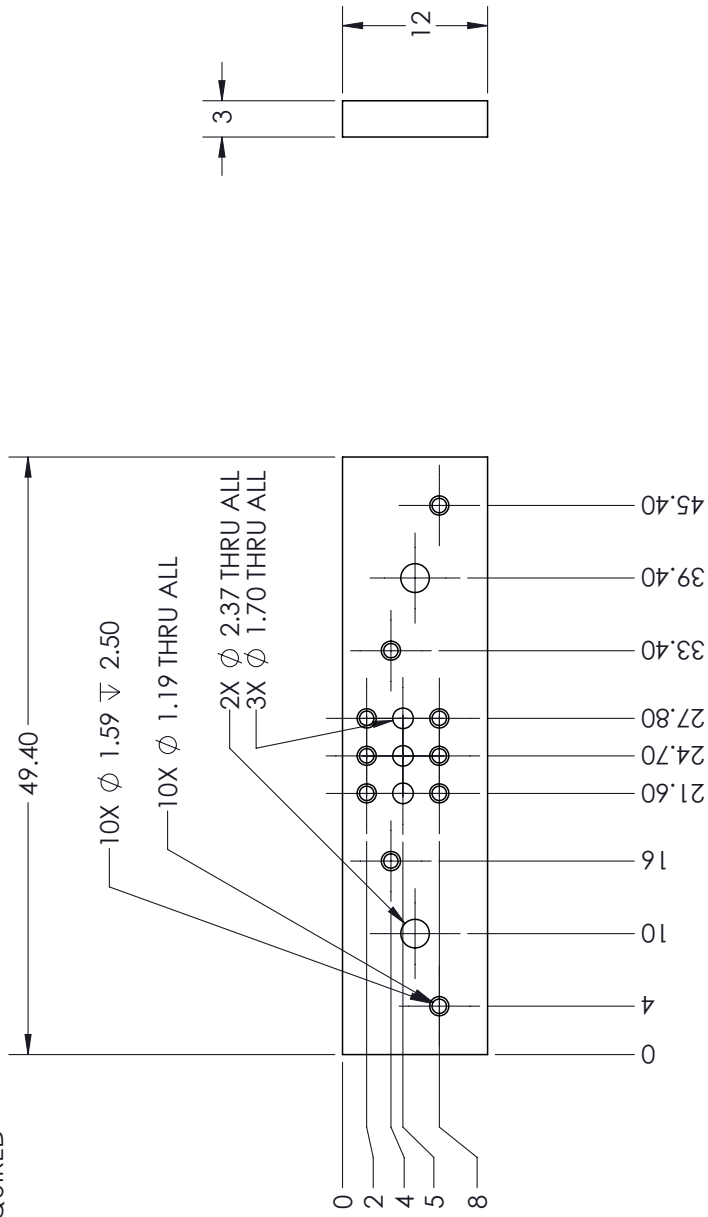
PHYSICS
DEPARTMENT
TITLE MACOR END
HOLE POSITIONS

SIZE	DWG. NO.	REV
A		
SCALE: 1:1	WEIGHT:	SHEET 6 OF 11

UNLESS OTHERWISE SPECIFIED: UNLESS OTHERWISE NOTED DIMENSIONS ARE IN MM TOLERANCES: ANGULAR: MACH $\pm .5^\circ$ BEND $\pm .5^\circ$ TWO PLACE DECIMAL $\pm .025$ MM THREE PLACE DECIMAL $\pm .013$ MM	NAME JMK	DATE 10/26/12
INTERPRET GEOMETRIC TOLERANCING PER:	DRAWN	CHECKED
MATERIAL MACOR	APPR	
FINISH		

DO NOT SCALE DRAWING

NOTES:
1. QUANTITY 2 REQUIRED



88

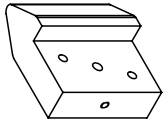
UNLESS OTHERWISE SPECIFIED:
DIMENSIONS ARE IN MM
TOLERANCES:
ANGULAR: MACH $\pm .5^\circ$ BEND $\pm .5^\circ$
TWO PLACE DECIMAL $\pm .025$ MM
THREE PLACE DECIMAL $\pm .013$ MM



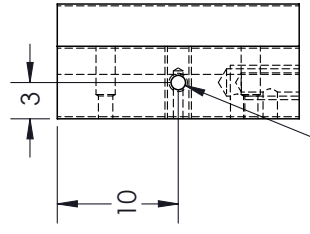
PHYSICS
DEPARTMENT
TITLE
MACOR BASE
SIZE DWG. NO. REV
A
SCALE: 2:1 WEIGHT: SHEET 7 OF 11

NAME DATE
JMK 10/26/12
DRAWN CHECKED
APPR

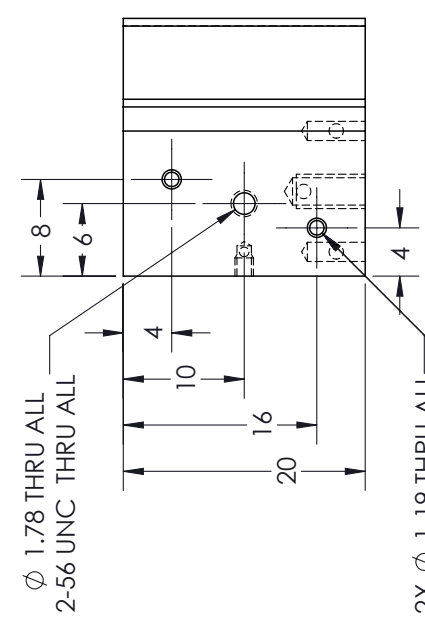
MATERIAL
MACOR
FINISH
DO NOT SCALE DRAWING



NOTES:
1. QUANTITY 4 REQUIRED

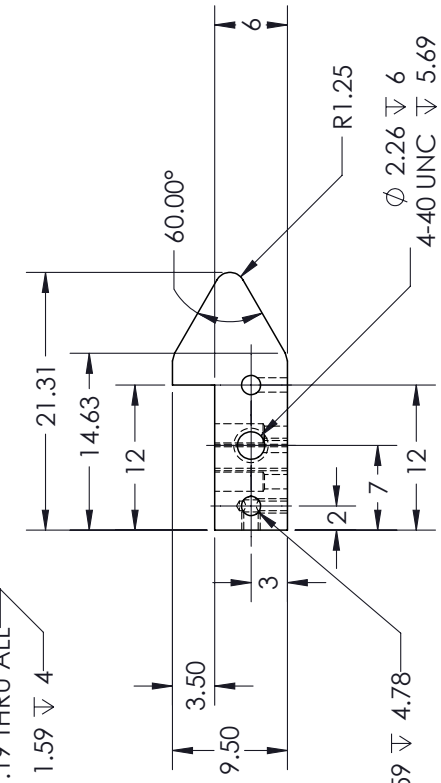


ϕ 1.19 ∇ 2.50
0-80 UNF ∇ 1.50



ϕ 1.78 THRU ALL
2-56 UNC THRU ALL

2X ϕ 1.19 THRU ALL
2X ϕ 1.59 ∇ 4



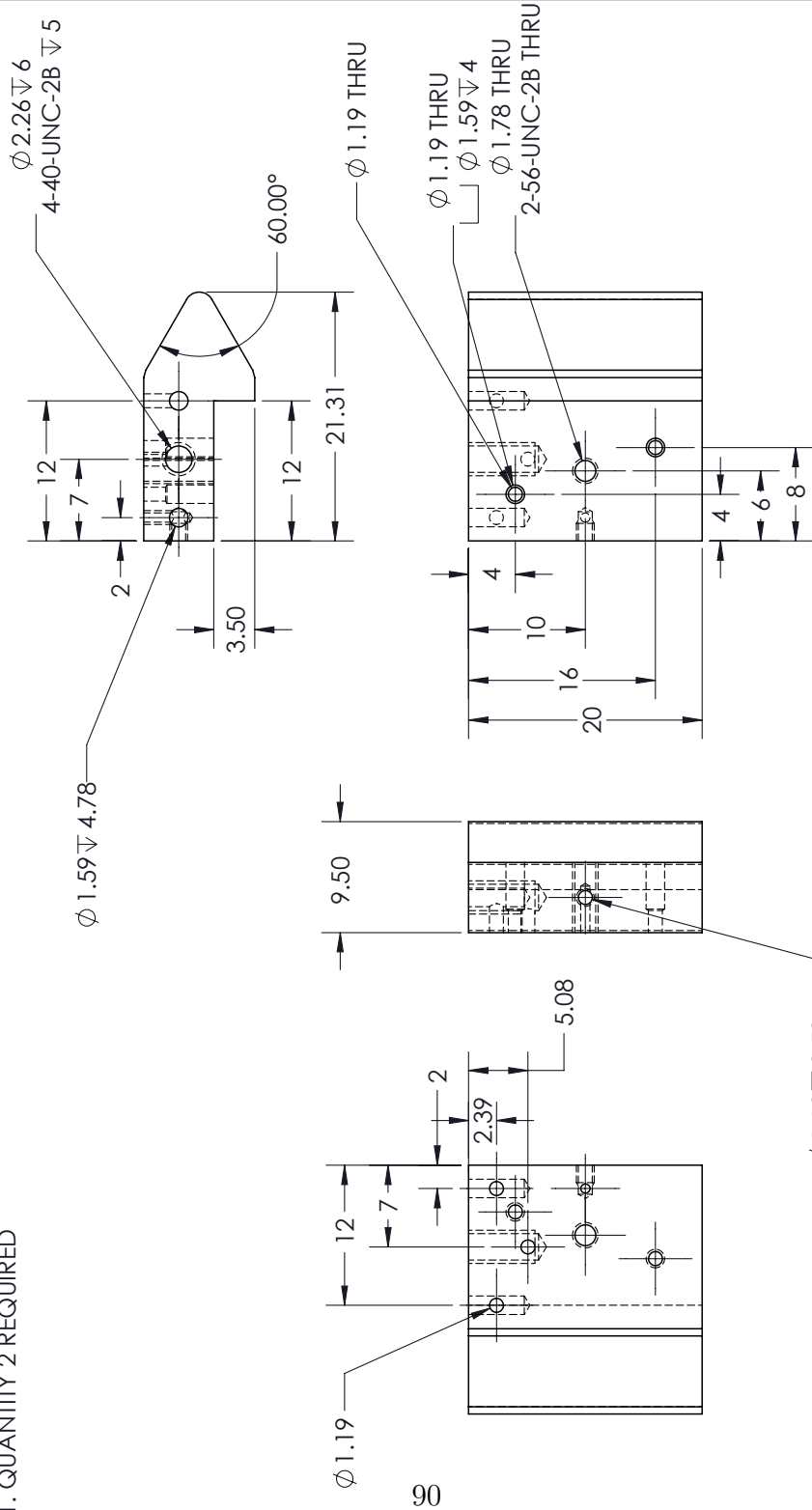
2X ϕ 1.59 ∇ 4.78
 ϕ 2.26 ∇ 6
4-40 UNC ∇ 5.69

UNLESS OTHERWISE SPECIFIED:
DIMENSIONS ARE IN MM
TOLERANCES:
ANGULAR: MACH \pm .5° BEND \pm .5°
TWO PLACE DECIMAL \pm .025MM
THREE PLACE DECIMAL \pm .013MM
INTERPRET GEOMETRIC TOLERANCING PER:
MATERIAL: OFHC COPPER
FINISH:
DO NOT SCALE DRAWING

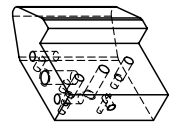
NAME	DATE	SIZE	DWG. NO.	REV
JMK	10/26/12	A		
DRAWN	CHECKED	APPR	SCALE: 2:1	WEIGHT:
				SHEET 8 OF 11

PHYSICS DEPARTMENT
TITLE: ELECTRODE W (top)

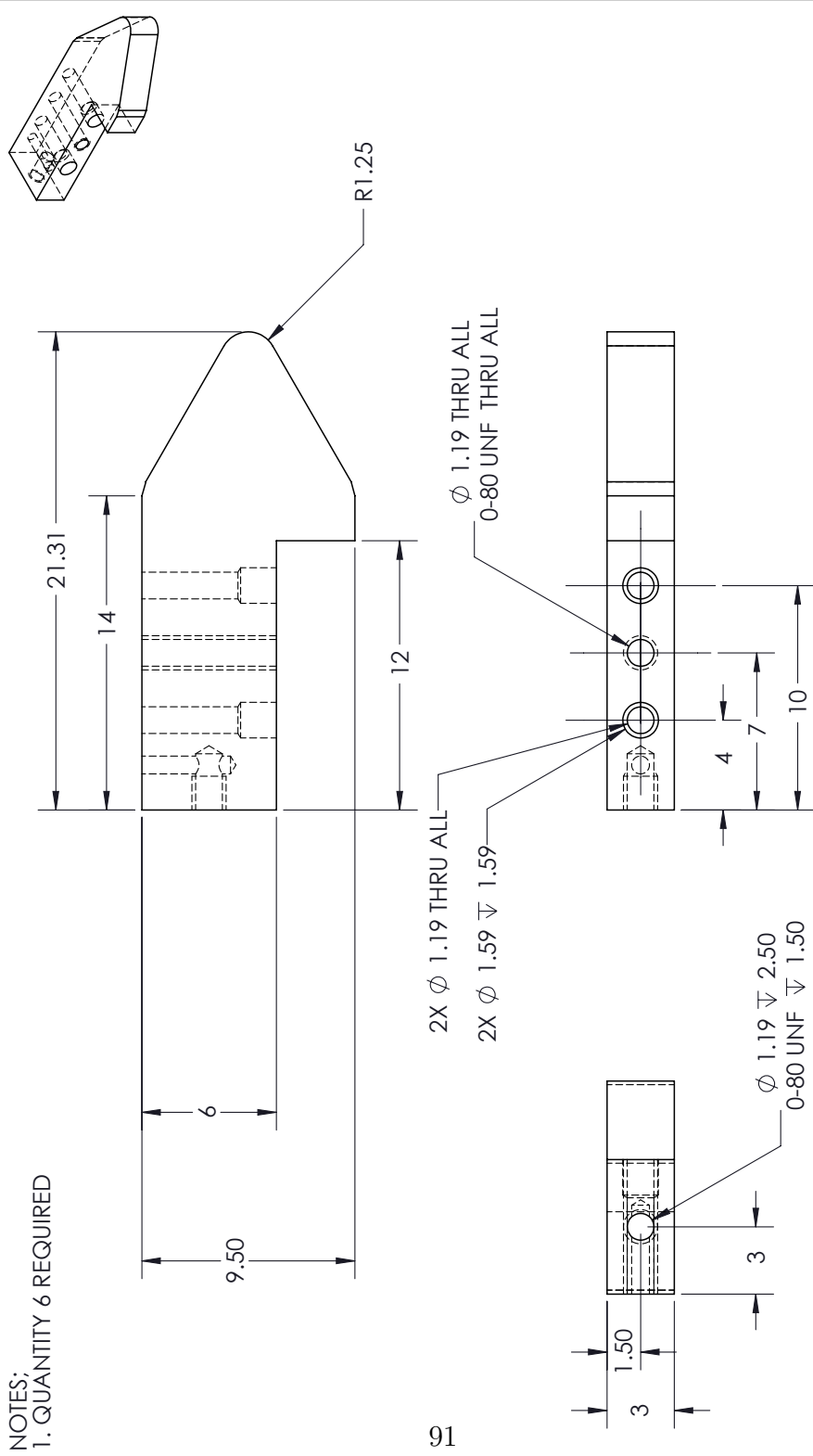
NOTES:
1. QUANTITY 2 REQUIRED



UNLESS OTHERWISE SPECIFIED: DIMENSIONS ARE IN INCHES				PHYSICS DEPARTMENT ELECTRODE W TOP	
TOLERANCES: FRACTIONAL ±1/64" ANGULAR: MACH ±.5° BEND ±.5° TWO PLACE DECIMAL ±.010" THREE PLACE DECIMAL ±.005" INTERPRET GEOMETRIC TOLERANCING PER:		NAME: JMK DATE: 11/1/12		SIZE: A DWG. NO.: REV:	
MATERIAL: OFHC COPPER FINISH:		DRAWN: JMK CHECKED:		SCALE: 2:1 WEIGHT:	
DO NOT SCALE DRAWING		APPR:		SHEET 9 OF 11	



NOTES:
1. QUANTITY 6 REQUIRED



91

		PHYSICS DEPARTMENT	
UNLESS OTHERWISE NOTED DIMENSIONS ARE IN MM TOLERANCES: ANGULAR: MACH $\pm .5^\circ$ BEND $\pm .5^\circ$ TWO PLACE DECIMAL $\pm .025$ MM THREE PLACE DECIMAL $\pm .013$ MM		ELECTRODE N	
INTERPRET GEOMETRIC TOLERANCING PER:		NAME: JMK	DATE: 10/26/12
MATERIAL: OFHC COPPER FINISH:		SIZE: A	DWG. NO.:
DO NOT SCALE DRAWING		DRAWN:	CHECKED:
APPR:		SCALE: 5:1	WEIGHT:
SHEET 10 OF 11		1	

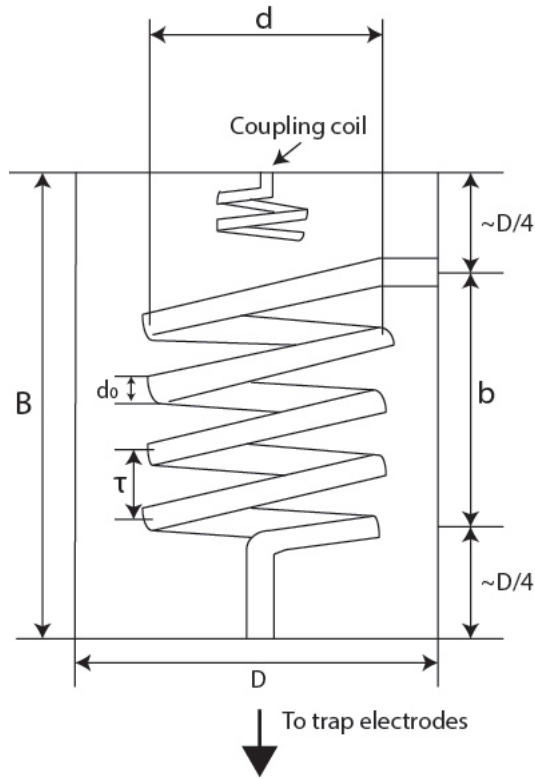
Appendix B

Mathematica Notebook for Helical Resonator

The RF Resonator Design Notebook

This Notebook is used for steps that leads to a complete helical resonator with a desirable RF resonance frequency and a large if not maximized Q. There are four steps to complete before you ending up with a functional product. All calculations are based on “On the application of radio frequency voltage to ion traps via helical resonators”, by Siverns et al. (Appl Phys B, DOI 10.1007/s00340-011-4837-0) Initial inputs are parameters of resonator A in table 2.

The picture below shows parameters of the resonator.



Step 1: Measure $C_{\Sigma} = C_t + C_w$ and $R_{\Sigma} = R_t + R_j$

$C_{\Sigma} = C_t + C_w$: the capacitance of the trap we have built and the capacitance of the wires connecting the resonator to the trap.

$R_{\Sigma} = R_t + R_j$: the resistance of the trap and the resistance of the solder joints. These numbers need to be measured with the vacuum feedthrough joined to the trap electrodes, properly grounded with all other in-vacuum circuit components.

$$C_t = 15 * 10^{-12};$$

$$C_w = 0.1 * 10^{-12};$$

$$C_{\Sigma} = C_t + C_w;$$

$$R_t = 5;$$

$$R_j = 0.5;$$

$$R_\Sigma = R_t + R_j;$$

Step 2: Calculate the combination $\{d/D, d\}$ that will maximize the Q of the system

d: the diameter of the inside coil of the resonator

D: the diameter of the outside shield

ρ : the resistivity of copper

δ : skin-depth

b[x,d]: the height of the coil as a function of $\{d/D, d\}$ (x replace d/D in the calculation below)

This calculation is done given the resonance frequency (ω_0) we want, the diameter of the wire used for the coil (d_0 , typically 5mm) and the winding pitch of the coil (τ , typically $2d_0$).

In order to get the desirable combination of $\{d/D, d\}$, read off from the contour plot the numbers corresponding to maximum Q (or a fairly large Q). We can then obtain d and D.

$$d_0 = 5 * 10^{-3};$$

$$\tau = 10 * 10^{-3};$$

$$\omega_0 = 10 * 10^6 * 2 * \pi;$$

$$\rho = 1.68 * 10^{-8};$$

$$KCs[x, d] := 39.37 * 0.75 / \text{Log}[1/x] * 10^{-12};$$

$$KLc[x, d] := 39.37 * (0.025 * d^2 * (1 - x^2)) / \tau^2 * 10^{-6};$$

```

b[x_, d_.]:= (C $\Sigma$  + Kcd[x, d]) / (KCs[x, d] + Kcb) *
(Sqrt [(KCs[x, d] + Kcb) / ((C $\Sigma$  + Kcd[x, d]) ^2 * KLC[x, d] *  $\omega$ 0^2) + 1/4] - 1/2)
Cs[x_, d_.]:=b[x, d] * KCs[x, d]
Cc[x_, d_.]:=b[x, d] * Kcb + Kcd[x, d]
n[x_, d_.]:=b[x, d]/ $\tau$ 
lc[x_, d_.]:=Sqrt[ $\tau$ ^2 + ( $\pi$  * d)^2] * n[x, d]
Ns[x_, d_.]:=b[x, d] * lc[x, d]/(4 *  $\pi$  * (d/x - d)^2)
ls[x_, d_.]:=Ns[x, d] * Sqrt[ $\pi$ ^2 * (d/x)^2 + (b[x, d]/Ns[x, d])^2]
Rs[x_, d_.]:=Ns[x, d] *  $\rho$  * ls[x, d]/(b[x, d] *  $\delta$ )
Rc[x_, d_.]:= $\rho$  * lc[x, d]/(d0 *  $\pi$  *  $\delta$ )
a[x_, d_.]:=Ct/(Cw + Cs[x, d])
 $\alpha$ [x_, d_.]:=a[x, d]/(a[x, d] + 1)
Resr[x_, d_.]:=Rs[x, d] + Rc[x, d] + Rj + Rt *  $\alpha$ [x, d]^2
Lc[x_, d_.]:=b[x, d] * KLC[x, d]

```

```
ContourPlot[{{Q[x, d]}, {x, 0, 1}, {d, 0, 0.2}, AxesLabel -> {"d/D", d}]
```

Step 3: Caculate the coil height b and other parameters and then

From b[x,d], by filling in the combination {d/D, d} chosen in step 2. I have hightlighted the parts that one needs to changes every time a new combination {d/D, d} is chosen.

We should set the shield height, B, to be b+D/2 (D1 replaces D here as D is protected by *Mathematica*).

```
Q[0.4, 0.07]
```

```
b[0.4, 0.07]
```

$$D1 = 0.07/0.4$$

$$B = b[0.4, 0.07] + D1/2$$

$$185.338$$

$$0.22775$$

$$0.175$$

$$0.31525$$

Step 4: Figure out antenna or coupling coil parameters

Z_{in} , the combined impedance of the resonator and the trap, must match that of the source of RF signal, which is the standard 50Ω . Solving for L_a (by equation (14) in Siverns) gives us some information about the antenna coil as we can model L_a by $L_a = \mu_0 N A / \tau_a$, where τ_a is the winding pitch of the antenna coil, N the number of turns and A the cross-sectional area.

Here we have arbitrarily chosen the diameter of the wire that makes up the antenna coil, d_a , to be 3.5 m and N (N1 replace N here) to be 3. Again, for easy hand-winding, we choose τ_a to be twice d_a .

k is the coupling constant, which is in the range of $0 \sim 1$. Here we assume it to be 0.1.

Notice that I have modeled Z_L , the impedance of the load, after the circuit analysis in section 3.2 of Siverns et al. For details, see lab log page 41.

The number calculated in the end is the diameter of the coupling coil that will impedance match the source and the load, which consists of the resonator and the trap.

$$N1 = 3;$$

$$da = 3.5 * 10^{-3};$$

```

τa = 2 * da;
Xc[x.]:=1/(x * ω0);
XL[x.]:=ω0 * x;
Zt[x., d.]:= (1/(i * Xc[Ct] + Rt) + 1/(i * Xc[Cw]) + 1/(i * Xc[Cs[x, d]]))^ - 1 + Rj + Rs[x, d];
ZL[x., d.]:= (1/Zt[x, d] + 1/(i * Xc[Cc[x, d]]))^ - 1 + Rc[x, d];
k = 0.1;
Soln = Solve[x * Abs[(i * ω0 + k^2 * Lc[0.4, 0.07] * ω0^2/(i * ω0 * Lc[0.4, 0.07] + ZL[0.4, 0.07]))] ==
x];
La = (x/.Soln[[1]]);
μ0 = 1.25663706 * 10^ - 6;
A = La/(μ0 * N1) * τa;
Sqrt[A/π] * 2
0.0434833

```

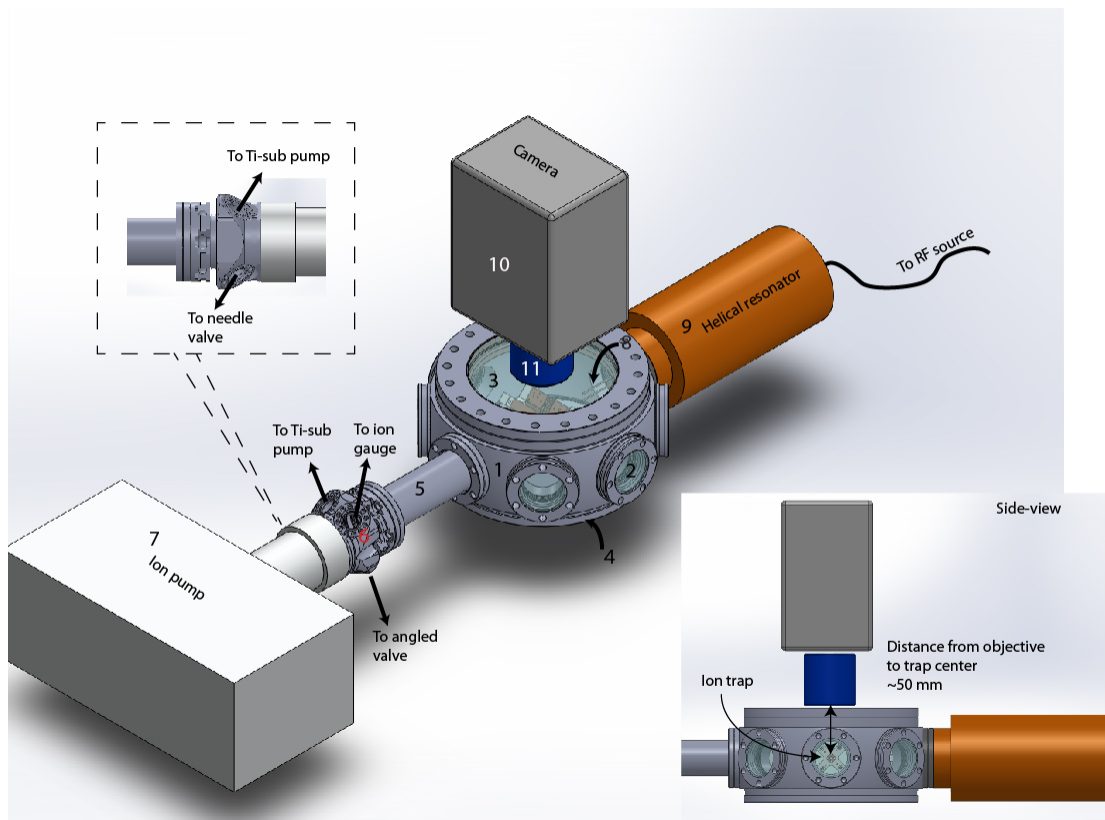
Final Step: Build resonator, test, and adjust.

Rules of thumb

- If resonance frequency is too large, we may be able to tune it by stretching the coil length (how ever this effect of stretching may be canceled out by the increase in winding pitch of the coil. We will see by experimenting.).
- Larger wire diameter for making the coil tends to lead to larger Q.
- If impedance of load (trap + resonator) is too high compared to RF source, stretch the antenna coil to increase its winding pitch and reduces the load impedance. If otherwise, do the opposite.

Appendix C

Inventory for Vacuum System



No.	Part
1	Vacuum chamber, Kimball Physics MCF800-SphOct-G2C8
2	2.75" CF viewport, Kimball Physics or Kurt J. Lesker or Nor-Cal
3	8" CF viewport, Kimball Physics or Kurt J. Lesker or Nor-Cal
4	CF flange with multi-pin connector, Kurt J. Lesker IFDGG501056B
5	Full nipple, Kurt J. Lesker FN-0275S
6	CF multiplexer, Kimball Physic MCF275-FlgMplx-C1r1A4
7	Ion pump, Agilent VacIon Plus 40-75
8	RF power feedthrough, Kurt J. Lesker FTT1023253
9	Helical resonator, "home-made"
10	Camera, Andor iXon3-885 DU-885K-CS0-#VP
11	Objective, custom-made

Bibliography

- [1] W. Paul, “Electromagnetic traps for charged and neutral particles,” *Rev. Mod. Phys.* **62**, 531 (1990).
- [2] F. G. Major, V. N. Gheorghe, and G. Werth, *Charged Particle Traps Physics and Techniques of Charged Particles Field Confinement* (Springer, New York, 2004).
- [3] D. Leibfried, R. Blatt, C. Monroe, and D. Wineland, “Quantum dynamics of single trapped ions,” *Rev. Mod. Phys.* **75**, 281 (2003).
- [4] F. W. J. Olver, D. W. Lozier, R. F. Boisvert, and C. W. Clark, *NIST Handbook of Mathematical Functions* (Cambridge University Press, New York, 2010).
- [5] J. D. Jost, *Entangled Mechanical Oscillators*, Ph.D. thesis, University of Colorado, Boulder (2001).
- [6] M. G. Raizen, J. M. Gilligan, J. C. Bergquist, W. M. Itano, and D. J. Wineland, “Ionic crystals in a linear Paul trap,” *Phys. Rev. A* **45**, 6493 (1992).

- [7] S. Geber, *Quantum Correlation Experiments with Resonance Fluorescence Photons of Single Barium Ions*, Ph.D. thesis, University of Innsbruck (2010).
- [8] K. Mølhave and M. Drewsen, “Formation of translationally cold MgH^+ and MgD^+ molecules in an ion trap,” *Phys. Rev. A* **62**, 011401 (2000).
- [9] R. Bowler, J. Gaebler, Y. Lin, T. R. Tan, D. Hanneke, J. D. Jost, J. P. Home, D. Leibfried, and D. J. Wineland, “Coherent Diabatic Ion Transport and Separation in a Multizone Trap Array,” *Phys. Rev. Lett.* **109**, 080502 (2012).
- [10] J. Siverns, L. Simkins, S. Weidt, and W. Hensinger, “On the application of radio frequency voltage to ion trap via helical resonators,” *Appl. Phys. B* **106** (2012).
- [11] J. F. O’Hanlon, *A User’s Guide to Vacuum Technology* (Wiley-Interscience, New York, 2003), 3rd ed.
- [12] T. Delchar, *Vacuum Physics and Techniques* (Chapman Hall, London, 1993).
- [13] A. Chambers, R. Fitch, and B. Halliday, *Basic Vacuum Technology* (IOP Publishing, London, 1998), 2nd ed.
- [14] G. Weston, *Ultrahigh Vacuum Practice* (Butterworth, London, 1985).
- [15] J. A. Venables, *Introduction to Surface and Thin Film Processes* (Cambridge University Press, Cambridge, 2000).

- [16] K. M. Birnbaum, *Cavity QED with Multilevel Atoms*, Ph.D. thesis, California Institute of Technology (2005).
- [17] J. Britton, *Microfabrication of Trapped-Ion Qubits within a Scalable Quantum Processor*, Ph.D. thesis, University of Colorado, Boulder (2008).
- [18] J. P. Home, D. Hanneke, J. D. Jost, D. Leibfried, and D. Wineland, “Normal modes of trapped ions in the presence of anharmonic trap potentials,” *New Journal of Physics* **13** (2011).
- [19] G. Morigi and H. Walther, “Two-species coulomb chains for quantum information,” *Eur. Phys. J. D* **3**, 261 (2001).
- [20] T. Chiba, “The Constancy of the Constants of Nature,” (2011), 1111.0092.
- [21] P. A. M. Dirac, “Cosmological Models and the Large Numbers Hypothesis,” *Proceedings of the Royal Society of London. A. Mathematical and Physical Sciences* **338**, 439 (1974).
- [22] P. Sisterna and H. Vucetich, “Time variation of fundamental constants. II. Quark masses as time-dependent parameters,” *Phys. Rev. D* **44**, 3096 (1991).
- [23] J.-P. Uzan, “The fundamental constants and their variation: observational and theoretical status,” *Rev. Mod. Phys.* **75**, 403 (2003).
- [24] W. J. Marciano, “Time Variation of the Fundamental ”Constants” and Kaluza-Klein Theories,” *Phys. Rev. Lett.* **52**, 489 (1984).

- [25] D. Griffiths, *Introduction to Elementary Particles* (Wiley-VCH, Weinheim, 2008), 2nd ed.
- [26] R. Thompson, “The Determination of the Electron to Proton Inertial Mass Ratio via Molecular Transitions,” *Astrop. Lett.* **16**, 3 (1975).
- [27] J. C. Berengut and V. V. Flambaum, “Astronomical and laboratory searches for space-time variation of fundamental constants,” (2010), 1009.3693.
- [28] J. Bagdonaite, P. Jansen, C. Henkel, H. L. Bethlem, K. M. Menten, and W. Ubachs, “A Stringent Limit on a Drifting Proton-to-Electron Mass Ratio from Alcohol in the Early Universe,” *Science* **339** (2013), ISSN 1095-9203.
- [29] N. Kanekar, “Constraining Changes in the Proton-Electron Mass Ratio with Inversion and Rotational Lines,” *Astrophysical Journal* **728** (2011).
- [30] A. Shelkovich, R. J. Butcher, C. Chardonnet, and A. Amy-Klein, “Stability of the Proton-to-Electron Mass Ratio,” *Phys. Rev. Lett.* **100**, 150801 (2008).
- [31] E. Reinhold, R. Buning, U. Hollenstein, A. Ivanchik, P. Petitjean, and W. Ubachs, “Indication of a Cosmological Variation of the Proton-Electron Mass Ratio Based on Laboratory Measurement and Reanalysis of H_2 Spectra,” *Phys. Rev. Lett.* **96**, 151101 (2006).
- [32] V. V. Flambaum and M. G. Kozlov, “Enhanced Sensitivity to the

- Time Variation of the Fine-Structure Constant and m_p/m_e in Diatomic Molecules,” *Phys. Rev. Lett.* **99**, 150801 (2007).
- [33] M. T. Murphy, V. V. Flambaum, S. Muller, and C. Henkel, “Strong Limit on a Variable Proton-to-Electron Mass Ratio from Molecules in the Distant Universe,” *Science* **320**, 1611 (2008), [arXiv/0806.3081](#).
- [34] T. Zelevinsky, S. Kotochigova, and J. Ye, “Precision Test of Mass-Ratio Variations with Lattice-Confined Ultracold Molecules,” *Phys. Rev. Lett.* **100**, 043201 (2008).
- [35] D. DeMille, S. Sainis, J. Sage, T. Bergeman, S. Kotochigova, and E. Tiesinga, “Enhanced Sensitivity to Variation of m_e/m_p in Molecular Spectra,” *Phys. Rev. Lett.* **100**, 043202 (2008).
- [36] S. Blatt, A. D. Ludlow, G. K. Campbell, J. W. Thomsen, T. Zelevinsky, M. M. Boyd, J. Ye, X. Baillard, M. Fouche, R. Le Targat, A. Brusch, P. Lemonde, *et al.*, “New Limits on Coupling of Fundamental Constants to Gravity Using ^{87}Sr Optical Lattice Clocks,” *Phys. Rev. Lett.* **100**, 140801 (2008).
- [37] T. M. Fortier, N. Ashby, J. C. Bergquist, M. J. Delaney, S. A. Diddams, T. P. Heavner, L. Hollberg, W. M. Itano, S. R. Jefferts, K. Kim, F. Levi, L. Lorini, *et al.*, “Precision Atomic Spectroscopy for Improved Limits on Variation of the Fine Structure Constant and Local Position Invariance,” *Phys. Rev. Lett.* **98**, 070801 (2007).
- [38] K. P. Huber and G. Herzberg, *Molecular Spectra and Molecular Structure*.

IV. Constants of Diatomic Molecules (Van Nostrand Reinhold Company, New York, 1979).

- [39] P. O. Schmidt, T. Rosenband, C. Langer, W. M. Itano, J. C. Bergquist, and D. J. Wineland, “Spectroscopy Using Quantum Logic,” *Science* **309**, 749 (2005).
- [40] J. D. Weinstein, R. Decarvalho, T. Guillet, B. Friedrich, and J. M. Doyle, “Magnetic trapping of calcium monohydride molecules at millikelvin temperatures,” *Nature* **395**, 148 (1998).
- [41] P. Blythe, B. Roth, U. Fröhlich, H. Wenz, and S. Schiller, “Production of Ultracold Trapped Molecular Hydrogen Ions,” *Phys. Rev. Lett.* **95**, 183002 (2005).
- [42] D. Leibfried, “Quantum state preparation and control of single molecular ions,” *New Journal of Physics* **14**, 023029 (2012).